Variations in kinase and effector signaling logic in a two component signaling network

Danielle Swingle[1,2], Leah Epstein[1,2], Ramisha Aymon[1,3], Eta A. Isiorho[1], Rinat R. Abzalimov[1], Denize C. Favaro[1], Kevin H. Gardner[1,3,4*]

[1]: Structural Biology Initiative, CUNY Advanced Science Research Center, New York, NY 10031

[2]: Ph.D. Program in Biochemistry, The Graduate Center – City University of New York, New York, NY 10016

[3]: Department of Chemistry and Biochemistry, City College of New York, New York, NY 10031

[4]: Ph.D. Programs in Biochemistry, Biology, and Chemistry, The Graduate Center – City University of New York, New York, NY 10016

*: direct correspondence to kgardner@gc.cuny.edu

ORCIDs:

Danielle Swingle: 0000-0003-3691-4560 / Leah Epstein: 0009-0004-9282-0715 / Ramisha Aymon: 0009-0003-0781-4760 / Eta A. Isiorho: 0000-0002-6242-9297 / Rinat R. Abzalimov: 0000-0003-2110-1532 / Denize C. Favaro: 0000-0001-5563-2548 / Kevin H. Gardner: 0000-0002-8671-2556

Classification: Biological Sciences / Biochemistry

Keywords: histidine kinase, bacterial signal transduction, general stress response, protein structure/function, two-component system

Running title: Variations in two component kinase and effector signaling logic

Abstract

The general stress response (GSR) protects bacteria from a wide range of stressors. In *Alphaproteobacteria*, GSR activation is coordinated by HWE/HisKA2 family histidine kinases (HKs), which can exhibit non-canonical structure and function. For example, while most light-oxygen-voltage sensor-containing HKs are light activated dimers, the *Rubellimicrobium thermophilum* RT-HK has inverted “dark on, light off” signaling logic with a tunable monomer/dimer equilibrium. Here, we further investigate these atypical behaviors of RT-HK and characterize its downstream signaling network. Using hydrogen-deuterium exchange mass spectrometry, we find that RT-HK uses a signal transduction mechanism similar to light-activated systems, despite its inverted logic. Mutagenesis reveals that RT-HK autophosphorylates *in trans*, with changes to the Jα helix linking sensor and kinase domains affecting autophosphorylation levels. Exploring downstream effects of RT-HK, we identified two GSR genetic regions, each encoding a copy of the central regulator PhyR. *In vitro* measurements of phosphotransfer from RT-HK to the two putative PhyRs revealed that RT-HK signals only to one, and does so at an increased intensity in the dark, consistent with its reversed logic. X-ray crystal structures of both PhyRs revealed a substantial shift within the receiver domain of one, suggesting a basis for RT-HK specificity. We probed further down the pathway using nuclear magnetic resonance to determine that the single NepR homolog interacts with both unphosphorylated PhyRs, and this interaction is decoupled from activation in one PhyR. This work expands our understanding of HWE/HisKA2 family signal transduction, revealing marked variations from signaling mechanisms previously identified in other GSR networks.

Significance

The Alphaproteobacterial general stress response (GSR) crucially handles responses to an array of stressors. In a typical photosensitive GSR pathway, blue light illumination stimulates

53 light-oxygen-voltage histidine kinase (LOV-HK) phosphorylation of a single PhyR response
54 regulator, regulating downstream stress gene transcription. The GSR regulators highlighted in
55 this study expand this signaling paradigm at three levels: 1) The LOV-HK RT-HK is dark-
56 activated, 2) only one of two PhyR homologs is apparently accessible to HK phosphodonors,
57 and 3) the other PhyR homolog shows negative cooperativity for activation and partner binding.
58 Our work enhances the current understanding of this complex stress response, introduces novel
59 regulatory modes, and underscores the necessity of testing structural and functional models
60 derived from homology.
61
62 **Introduction**
63 Bacteria are relatively simple organisms that directly face complex environmental
64 challenges, such as fluctuations in nutrient availability, osmolarity, pH, and temperature. To
65 sense and adapt to their changing surroundings, bacteria commonly use two-component
66 systems (TCSs), minimally comprised of a sensor histidine kinase (HK) and cognate response
67 regulator (RR)[3,4]. Signal input to the HK's sensor domain modulates autophosphorylation of a
68 conserved histidine residue within its dimerization and histidine phosphotransfer (DHp) domain
69 by an ATP molecule bound to its catalytic ATP-binding (CA) domain. This phosphoryl group is
70 subsequently transferred to a conserved aspartate residue within the receiver (REC) domain of
71 the RR. This relay ultimately affects cellular output, typically via RR-mediated transcription[5-7].
72 The vast number of HKs can be classified into families based chiefly on their primary
73 sequence features. Among these groupings, the lesser-studied HWE/HisKA2[8,9] superfamily is
74 distinguished by a motif near the phosphoacceptor histidine residue (H-box), a conserved
75 arginine (R-box), a long ATP lid, and a glutamate that replaces the first asparagine of the N-box.
76 These unique features evidently result in higher-order differences that further distinguish this
77 family. First, while canonical HKs are membrane-bound and strictly homodimeric, many of the
78 HWE/HisKA2 HKs characterized thus far are soluble and non-dimeric. This phenomenon is

79 exemplified most dramatically by the monomeric EL346[10] and the hexameric EsxG[11] proteins.
80 With only two full-length structures solved to date[10,12], there is still much to be learned about the
81 primary sequence features that underly higher order structural differences and how this family
82 fits into the broader structural picture of sensor HKs.

83 Another defining characteristic of HWE/HisKA2 family members is their involvement in
84 the general stress response (GSR) networks of *Alphaproteobacteria*[13-20]. The GSR is a gene
85 expression program that enables bacteria to cope with a range of adverse conditions such as
86 oxidative stress, heat shock, and UV exposure[2,13,21]. This response works using a so-called
87 "partner-switching" mechanism, whereby HK activity – and subsequent phosphorylation of a
88 downstream PhyR regulator[22-27] – controls the activity of a transcriptional inhibitor known as
89 NepR. In the absence of stress, transcription is prevented by NepR binding to the σ^{EcfG} general
90 transcription factor. Stress activates an HWE/HisKA2 HK, phosphorylating the PhyR and
91 promoting sequestration of NepR away from σ^{EcfG}, allowing transcription of stress-responsive
92 genes to occur. Details of the mechanism which links PhyR phosphorylation to NepR binding
93 remain unclear, as initial models[25,28] have proposed that phosphorylation of the PhyR REC
94 domain produces an open state that allows NepR to bind its σ-like (SL) domain, while more
95 recent studies suggest that nascent interaction of NepR with unphosphorylated PhyR precedes
96 PhyR phosphorylation and open state formation[29].

97 From this basic architecture, several variations on GSR signaling have been observed,
98 from multiple paralogous copies of various GSR key components[2,13,21,27,30-32] to differences in
99 the signaling logic of the histidine kinases which control pathway activity. One example of the
100 latter is provided by our prior work on a novel HWE/HisKA2 from *Rubellimicrobium*
101 *thermophilum* DSM 16684[33] called RT349[34] (referred to here as RT-HK). This protein contains a
102 light-oxygen-voltage (LOV)[14,35,36] sensor domain, which detects blue light via the photoreduction
103 of a bound flavin cofactor and concomitant formation of a covalent protein/flavin adduct. As

104 seen for some of its HWE/HisKA2 relatives, we determined that RT-HK is not strictly dimeric;
105 instead, its dimer-leaning equilibrium shifts towards more compact/monomeric conformations
106 under lit conditions and in the absence of ATP[34]. More unexpectedly, we found that its net
107 kinase activity is higher in the dark than in the light[34]. To our knowledge, RT-HK is the only
108 naturally occurring LOV-HK with its signaling logic inverted from the more standard light-
109 activated mode, though we note that genetic studies of *E. litoralis* DSM 8509 suggest the
110 presence of a dark-activated GSR under partial control of a LOV-HK[37]. A similar inverted logic
111 has been conferred upon some engineered light-sensing HKs via alterations to the helical
112 linkers between the sensor and catalytic domains (stemming from the Jα helix in LOV systems),
113 but no generally applicable pattern for achieving this outcome has been established[38,39].
114 Here, we further investigated RT-HK's oligomeric state and reversed signaling logic, as
115 well as its downstream partners. We found that RT-HK likely uses a signal transduction
116 mechanism similar to light-activated systems, as well as an *in trans* mode of
117 autophosphorylation, and the length and register of its Jα linker can be altered to affect net
118 autophosphorylation levels. Exploring downstream effects of RT-HK, we identified two homologs
119 of PhyR in the genome, RT-PhyR and RT-PhyR′. *In vitro* phosphotransfer measurements
120 showed that RT-HK only specifically signals to RT-PhyR, and at an increased intensity in the
121 dark consistent with autophosphorylation levels. Crystal structures of both PhyR variants
122 uncovered a substantial structural shift in RT-PhyR′ immediately following its phosphorylation
123 site, suggesting a possible mechanism of RT-HK preference for RT-PhyR. Further down the
124 GSR pathway, we observed unexpected interaction modes between the single NepR homolog
125 and both unphosphorylated PhyRs, as the RT-PhyR':NepR interaction is decoupled from
126 phosphorylation, indicating a phosphorylation-independent function for this homolog. Thus, this
127 system exhibits signaling variations at three levels – HK reversed logic, HK phosphorylation of

128 RT-PhyR′, and binding of RT-PhyR′ to RT-NepR′ – that broaden our view of the signaling
129 paradigms in this class of bacterial two-component pathways.
130
131 **Results**
132 ***Light signal propagation in a dark-activated histidine kinase***
133 We set out to further investigate the inverted signaling logic and oligomeric state
134 equilibrium of RT-HK we previously identified[34], seeking to better characterize how RT-HK is
135 able to take the same light input as other studied natural LOV-HKs and return an opposite
136 output. In these systems, the light signal is propagated across a considerable distance of
137 approximately 60 Å from the flavin cofactor within the LOV domain to the ATP in the kinase
138 domain (**Figure 1a**). While the dynamics of light signaling have been examined in some LOV-
139 HKs[40-45], this is the first time it has been explored in a naturally occurring dark-activated system.
140 We began at the global level, using limited trypsinolysis to probe the accessibility of RT-HK
141 under different illumination conditions (dark vs. lit) and nucleotide states (apo vs. AMP-PNP-
142 bound). Using SDS-PAGE analyses of these experiments, we found that RT-HK is markedly
143 more protease-susceptible under lit than dark conditions (**Figure 1b**). More specifically,
144 quantitation of the intact protein band in these gels (**Figure 1c**) showed that both illumination
145 and nucleotide state influenced protein accessibility, with a rank order of protease stability being
146 lit apo > lit AMP-PMP > dark apo > dark AMP-PNP. This trend is reminiscent of that seen for
147 RT-HK oligomeric state, where the equilibrium was shifted towards monomer in the lit apo state
148 and dimer in the dark ATP state[34].
149 To further elucidate the relationship between RT-HK oligomeric state and activity, we
150 investigated the autophosphorylation mechanism, seeking to establish if this HK phosphorylates
151 its conserved phosphoacceptor His residue using the γ-phosphate of the ATP molecule bound
152 either to the same monomer subunit (*in cis*) or the opposite subunit (*in trans*). The mechanism

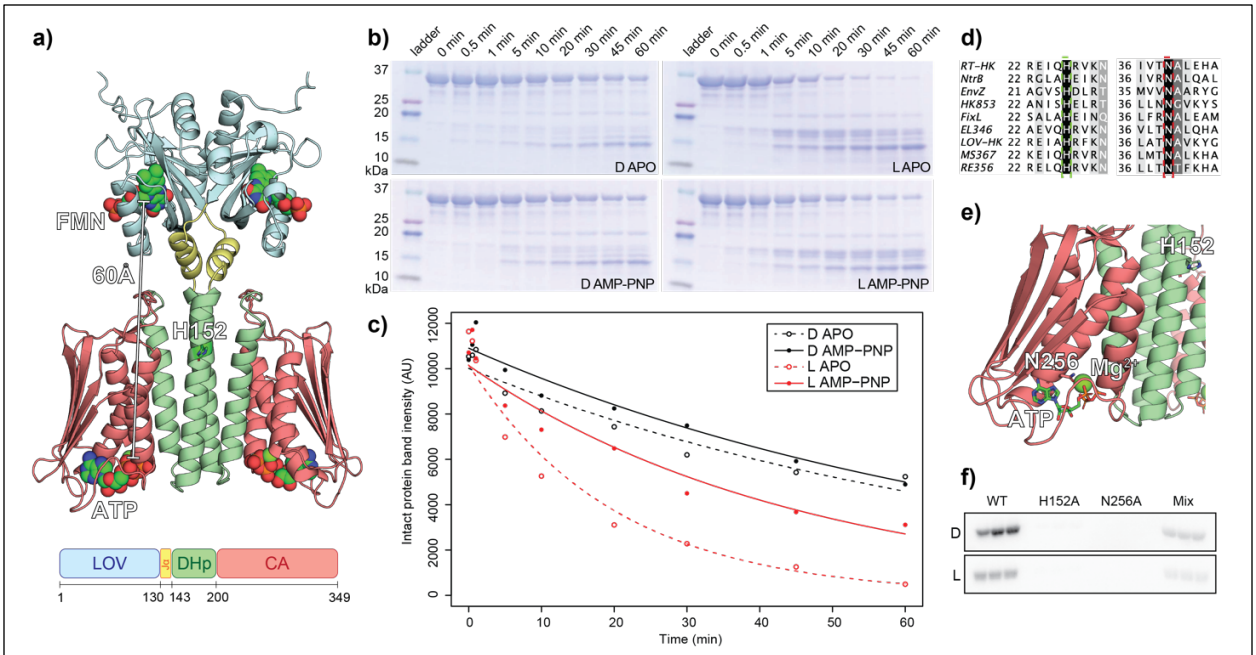

Figure 1: RT-HK protease accessibility is dependent on illumination and nucleotide-binding state, and autophosphorylates *in trans*. a) AlphaFold[1] model of dimeric RT-HK (top) and domain architecture (bottom) and with domains colored correspondingly. The predicted phosphoacceptor histidine residue is shown as sticks, and bound FMN and ATP molecules are shown as spheres, with the distance between them highlighted. **b)** SDS-PAGE gels showing trypsin cleavage pattern of RT-HK over time in dark, lit, apo, and AMP-PNP-bound states. **c)** Intensity of intact protein band over time, with points fit to an exponential curve. **d)** Multiple sequence alignment of RT-HK with other well-studied HKs. Dashed boxes are drawn around the predicted phosphoacceptor His and Mg-chelating Asn residues. **e)** RT-HK AlphaFold model with mutated H152 and N256 residues shown as sticks. **f)** Phosphoimaged SDS-PAGE gels of autophosphorylation assay reactions show substantial ^{32}P incorporation only in wild-type (WT) and H152A/N256A mixed (Mix) samples (n=3).

can be determined by assaying kinase activity on samples composed of a blend of two RT-HK variants which each contain one of two mutants, one deficient in the phosphoacceptor His residue and the other deficient in a conserved Mg^{2+}-chelating Asn. Neither of these mutants can autophosphorylate as a homodimer, but when the two are heterodimerized, activity will be restored only if the HK uses a *trans* mechanism[46]. We identified the appropriate RT-HK point mutations needed for this assay, H152A and N256A, by using a multiple sequence alignment[47] (**Figure 1d**) and predicted structural model[1] (**Figure 1e**). As expected, each of these mutants alone did not incorporate a measurable amount of ^{32}P from the γ-^{32}P-ATP substrate in autophosphorylation assays (**Figure 1f**), but we observed restored kinase activity in samples

162 mixing the two mutants. These results indicate that RT-HK autophosphorylates *in trans*.
163 Notably, we saw higher kinase activity of the mixed samples in the dark than in the light,
164 demonstrating that the signaling logic was not affected by the mutations.

165 The accessibility of RT-HK to hydrogen-deuterium exchange (HDX) was next assessed
166 at the peptide level using a mass spectrometry readout (HDX-MS). Exchange was measured in
167 six different states, varying lit and dark conditions of the LOV domain with either apo, ADP, or
168 AMP-PNP nucleotide states of the kinase domain. Mapping the difference in deuterium uptake
169 between lit and dark conditions in apo, AMP-PNP-, and ADP-bound nucleotide states onto the
170 RT-HK AlphaFold model (**Figure 2**) illustrates several key areas of difference. Intriguingly,
171 peptides throughout the LOV domain exhibited bimodal distributions (**Figure S1**), with an
172 increased ratio of the fast-exchanging population consistently present under lit conditions,
173 regardless of nucleotide state. For two LOV domain peptides with unimodal distributions (17-22
174 & 70-79) as well as a peptide in the Jα linker helix (127-148), we observed increased exchange
175 under lit conditions. These data are consistent with prior HDX studies of LOV domains and
176 proteins by NMR[48,49] or MS[50]. The pattern changes substantially in DHp and CA regions, where
177 nucleotide is essential for large-scale HDX. This is exemplified by a peptide from the DHp
178 region (182-189), which experienced similar exchange under dark and lit conditions in the apo
179 state but showed higher exchange in the dark once nucleotide was added. A peptide at the
180 interface between the DHp and CA (213-231) shows nucleotide dependence only in the light. In
181 the ATP lid region of the CA domain (286-315), the peptide shows decreased exchange when
182 AMP-PNP is bound, especially in the dark. Overall exchange in the DHp-CA domains is similar
183 between both nucleotide states, with ADP having a more muted effect. All-in-all, it is clear that
184 nucleotide is required for post-LOV signal transmission and the DHp is at the heart of this
185 process.

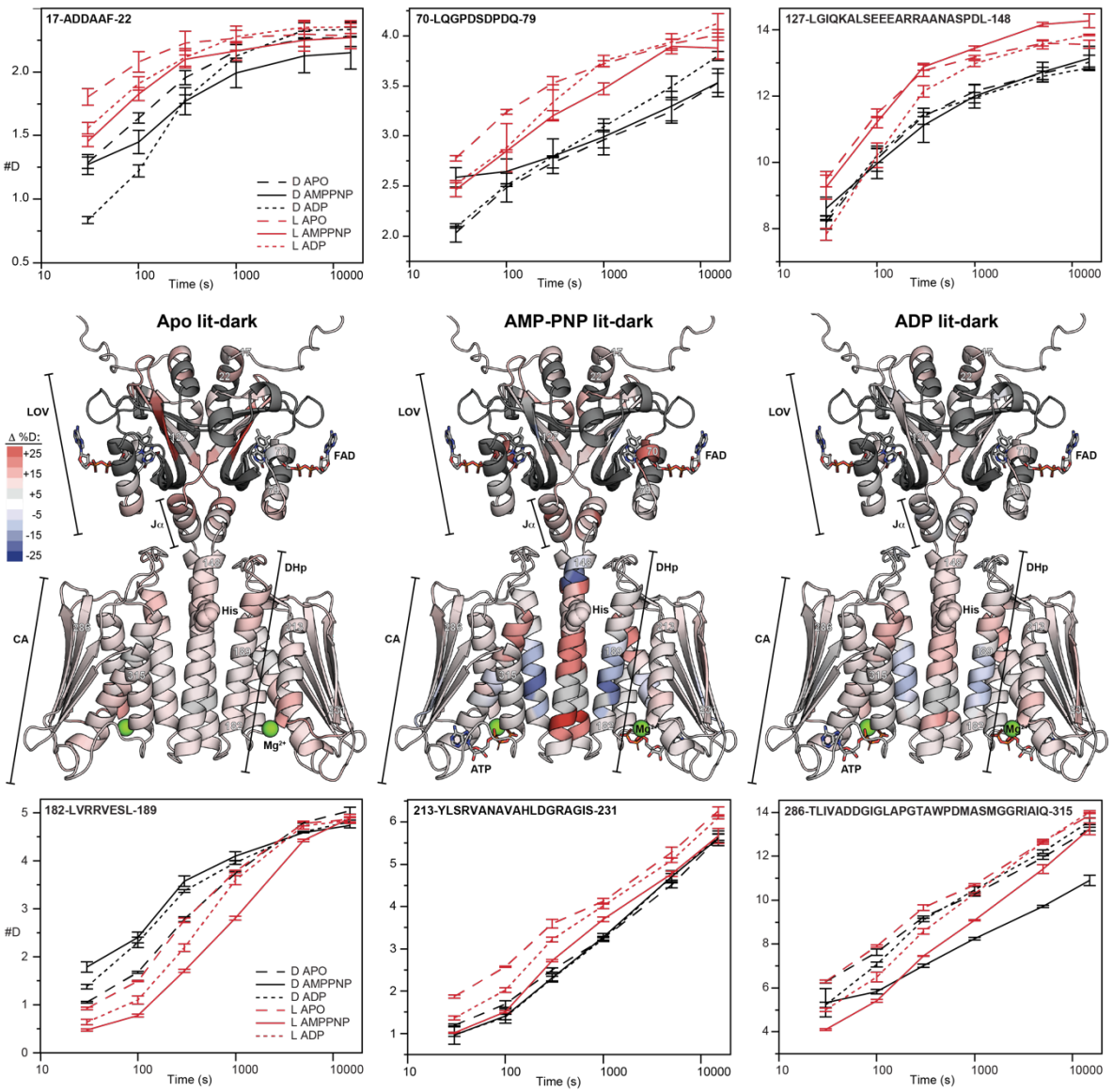

Figure 2: Different regions of RT-HK are differentially affected by light or nucleotide state as assayed by HDX-MS. RT-HK AlphaFold models are colored according to deuterium uptake differences (lit-dark %D) in apo, AMP-PNP-, and ADP-bound states at 300 s, with red (or blue) reflecting increased (or decreased) exchange in the light, respectively. Chiefly bimodal regions are colored dark grey. Uptake plots are shown for selected peptides whose positions are indicated by residue numbers on the models. Error bars represent standard deviation of 3 replicates.

Our HDX-MS results highlighted the importance of Jα-containing peptides in signal transduction, prompting us to look further into this region. Previous work on chimeric engineered light-sensing HKs has shown that altering the length of this helix can markedly affect how light

189 input controls net kinase activity[38,39,51]. This phenomenon is generally attributed to

190 conformational changes in the coiled-coil linker between the light-sensing and effector modules

191 of the HK. Intriguingly, the predicted RT-HK structural model has a pronounced break in the

192 coiled-coil between the Jα helix and DHp, likely caused by residue P143 (**Figure 3a**). Four

193 residues surrounding this region were systematically deleted and the effect on net kinase

194 activity was assessed *in vitro* using a γ-^{32}P-ATP substrate (**Figure 3b**).

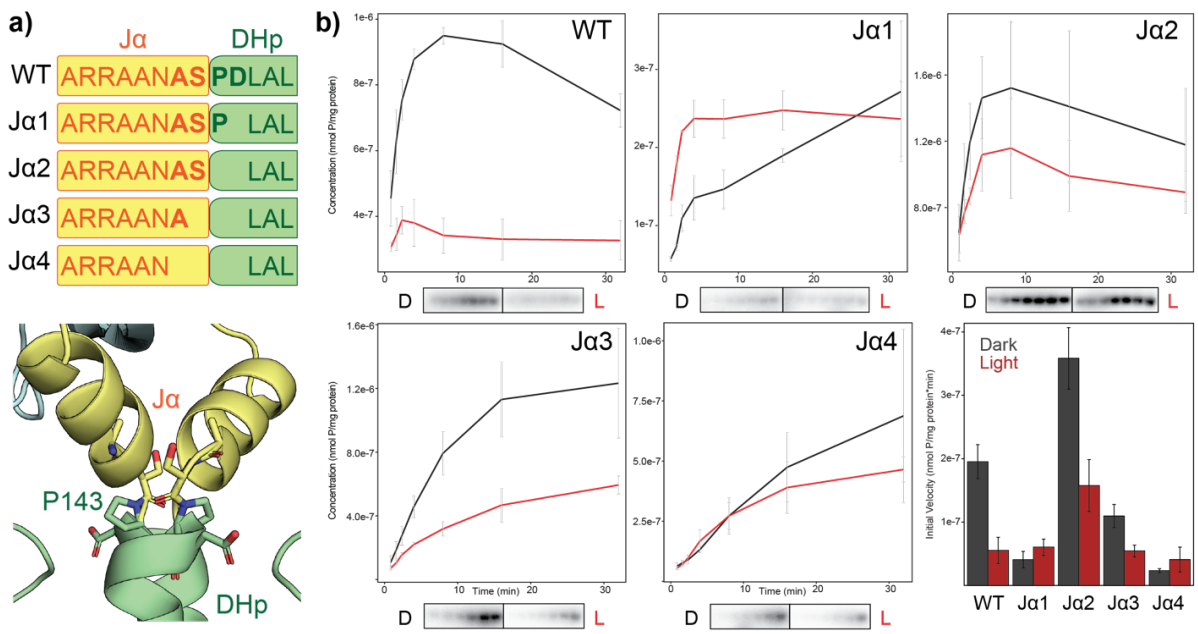

Figure 3: Deletions in Jα linker affect net RT-HK autophosphorylation levels and signaling logic. a) Schematic showing positions of amino acid deletions for each construct (top) and AlphaFold model of RT-HK with deleted residues shown as sticks (bottom). **b)** Autophosphorylation assays (plots above, phosphoimages below) are plotted as concentration vs. time for each protein, with dark measurements shown as black lines and lit shown in red. The bar plot shows the initial velocity measured from the linear portion of each curve, with dark measurements shown in dark grey and lit measurements in red. Each point/bar indicates the mean and all error bars span +/- one SD (n=3).

195 As expected, the wild-type RT-HK showed a sizeable increase in net

196 autophosphorylation in the dark state as compared to the lit state. Surprisingly, removing a

197 single residue to produce the Jα1 mutant caused a drop in dark state activity, resulting in a

198 modest reversal of the signaling logic. The next amino acid deletion (notably, the P143 residue

199 likely “kinking” this region) had the opposite effect – activity in both states increased greatly

200 compared to wild type and the reversed signaling logic was restored. The activity of Jα3 was
201 comparable to wild type, though attenuated in the dark state. And lastly, Jα4 showed a similar
202 effect to Jα1, with a sharp drop in net autophosphorylation levels and another slight reversal of
203 the signaling logic. All-in-all, these results suggest a helical-type periodicity of approximately 3.8
204 residues, highlighting the importance of the Jα helix and subsequent coiled coil in transmitting
205 signal between sensor and effector domains.
206
207 ***The role of a dark-activated LOV-HK in a paralogous GSR***
208 After investigating how the light signal propagates through the RT-HK molecule, we set
209 out to identify signaling partner/s and determine if the reversed logic is transferred downstream.
210 Recognizing that HWE/HisKA2 family HKs are often involved in the GSR[13-20], we searched the
211 *R. thermophilum* DSM 16684 genome for homologs of the key players: the sigma factor σ^{EcfG},
212 the anti-sigma factor NepR, and the anti-anti-sigma factor PhyR response regulator. This search
213 revealed two sets of GSR genes encoded in separate genomic loci, which we refer to as GSR
214 and GSR′ (**Figure 4a**). GSR′ exhibits the typical organization, containing one copy each of
215 NepR, PhyR, and σ^{EcfG} (RT-NepR′, RT-PhyR′, and RT-σ^{EcfG}'), as well as another HWE-family
216 HK (distinct from RT-HK). Surprisingly, the GSR region also contains its own copies of PhyR
217 and σ^{EcfG} (RT-PhyR and RT-σ^{EcfG}). It is uncommon to find multiple copies of GSR regulators
218 within a single organism and several studies have focused on this phenomenon[27,32,52].
219 With these two putative downstream PhyR partners in hand, we explored the ability of
220 RT-HK to phosphorylate each using an *in vitro* phosphotransfer assay[53] (**Figure 4b**). We
221 measured such phosphotransfer at two timepoints: a short timepoint (30 s) to identify the
222 kinetically preferred cognate partner, coupled with a longer timepoint (10 min) to characterize
223 any non-specific transfer. At the short timepoint, we observed transfer only to RT-PhyR,
224 suggesting that it is the cognate partner of RT-HK. Further, the intensity of the phosphorylated

225 RT-PhyR bands were higher in the dark condition at both timepoints, indicating RT-HK's
226 reversed logic had been transferred downstream. Notably, RT-PhyR′ was phosphorylated only
227 at the longer timepoint and without a marked illumination dependence, suggesting that it is a
228 non-specific partner.

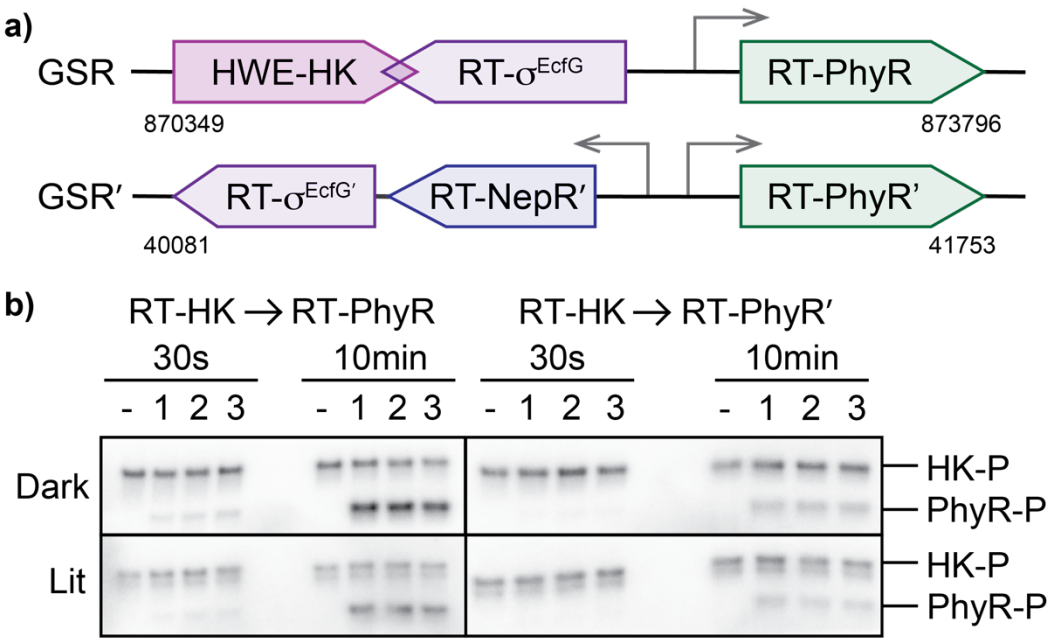

Figure 4: RT-HK reversed signaling logic is transferred to downstream partner RT-PhyR. a) Architecture of the two GSR loci in *R. thermophilum* DSM 16684 with genomic locations specified below. Arrows indicate open reading frames. Promoter regions (grey arrows) were predicted from the consensus sequence GGAAC-$N_{16\text{-}17}$-C/GGTT[2]. **b)** Phosphoimaged gels tracking the *in vitro* transfer of a ^{32}P-labeled phosphoryl group from RT-HK to RT-PhyR (left) and RT-PhyR′ (right). Experiments were performed in dark (top) and lit (bottom) conditions, and samples were taken at 30 s and 10 min timepoints. A negative control (phosphorylated RT-HK only) was run at each timepoint in the left-most lane and triplicate samples were run in consecutive lanes. The top band in each lane corresponds to the mass of phosphorylated RT-HK and bands below this correspond to the mass of the phosphorylated PhyR homolog.

229 Though there are clear differences between the ability of the two PhyR paralogs to
230 interact with RT-HK, the root of these differences is not immediately apparent from their primary
231 sequences, as they share 64% identity and generally align well with PhyRs from other
232 organisms (**Figure S2**). To provide a structural basis for RT-HK specificity among these two
233 related proteins, we solved the crystal structures of RT-PhyR (1.99 Å resolution; PDB ID: 9BY5)

234 and RT-PhyR′ (2.83 Å resolution; PDB ID: 9CB6); data collection and refinement statistics for

235 both structures are summarized in **Table S1**. RT-PhyR and RT-PhyR′ were solved as a

236 crystallographic trimer and a tetramer, respectively.

237 In the structures of both RT-PhyR (**Figure 5a**) and RT-PhyR′ (**Figure 5b**), we observed

238 a typical arrangement between the sigma-like (SL) and receiver (REC) domains. The fold of the

239 SL domain is a seven α-helical bundle consisting of the σ2 (α1-3) and σ4 (α5-7) regions, which

240 are connected by a disordered loop that includes α4. Unsurprisingly, no electron density was

241 present for the disordered loop in RT-PhyR′. However, we were able to model this loop into

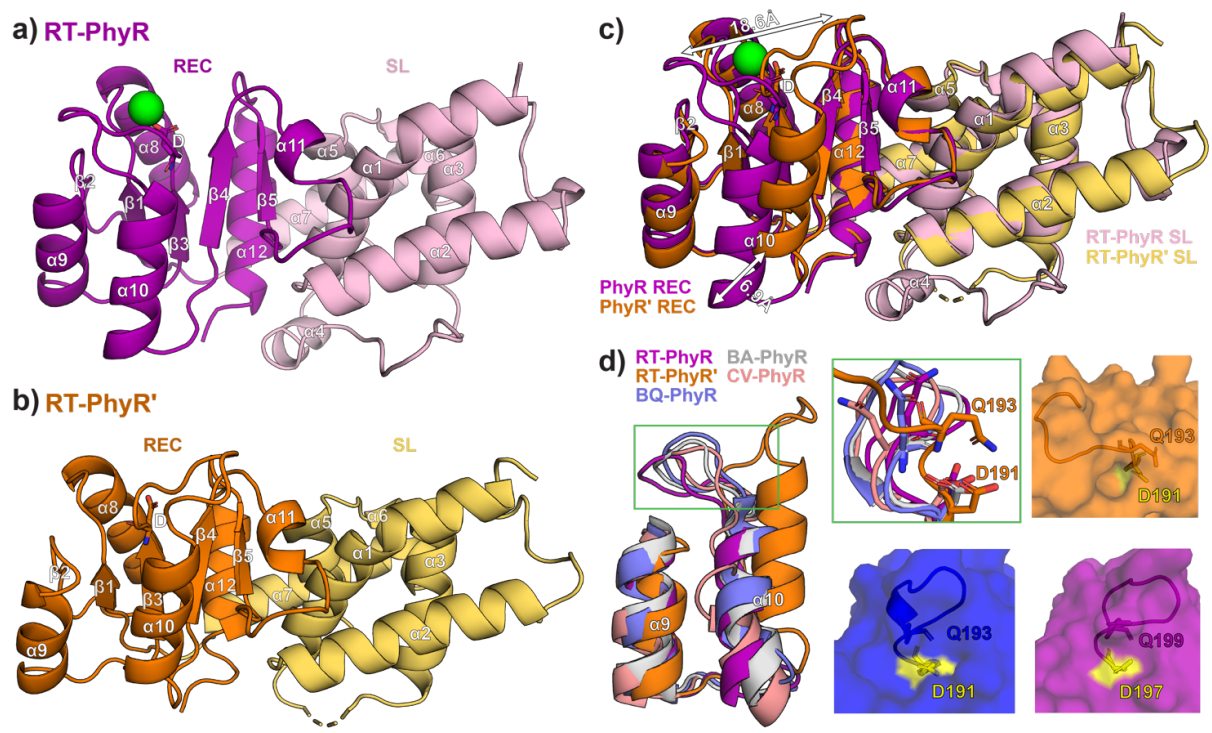

Figure 5: Comparisons of RT-PhyR and RT-PhyR′ crystal structures. a) RT-PhyR (PDB ID: 9BY5) and **b)** RT-PhyR′ (PDB ID: 9CB6) crystal structures with domains and secondary structure elements labeled. The phosphoacceptor D residues are shown as sticks. **c)** Aligned RT-PhyR and RT-PhyR′ crystal structures highlight differences in the position of the β3-α10 loop and α10 helix (white arrows). **d)** Aligning several known PhyR structures (labeled according to first two letters of their host organism; BQ PhyR: 5UXW, BA PhyR: 4G97, CV PhyR: 3N0R) to the RT-PhyR/RT-PhyR overlay illustrate that the RT-PhyR′ β3 loop–α10 helix position is the outlier. The green zoomed-in region highlights the unique position of Q193 in RT-PhyR′ near phosphoacceptor D191. Surface representation comparisons illustrate the limited solvent accessibility of D191 in RT-PhyR′.

242 monomer B of the RT-PhyR structure, where it adopts an atypical position (**Figure S3**). The C-
243 terminal end of the SL domain leads into the REC domain, which displays the canonical α/β fold
244 in both proteins.

245 Aligning the two PhyR paralog structures shows a reasonably high degree of overall
246 similarity (2.7 Å Cα RMSD) (**Figure 5c**), with a notable major shift in the position of the loop
247 connecting the β3 strand (immediately following the phosphoacceptor D residue) and
248 subsequent α10 helix (α3 in standard REC nomenclature). Adding other PhyR structures into
249 the alignment (**Figure 5c**), it is evident that RT-PhyR′ adopts an unusual conformation not
250 routinely seen in other REC domains. This large-scale shift in RT-PhyR′ is likely related to the
251 unique position of a conserved Q residue (Q193), which "leans in" and diminishes the solvent
252 accessibility of the phosphoacceptor D (D191) (**Figure 5d**). Two residues in the α9 helix of RT-
253 PhyR′ also adopt distinct positions: a well-conserved R at the N-terminus (R173) and another R
254 at the C-terminus (R184) "reach out" toward the typical position of the β3 loop and α10 helix,
255 respectively (**Figure S4**).

256 Continuing to the next steps of the signaling pathway, we used ^{15}N/^{1}H TROSY
257 experiments with uniformly ^{15}N-labeled RT-PhyR or RT-PhyR′ to investigate their functional
258 properties and interactions with the single *R. therm.* NepR homolog, RT-NepR′ (**Figure 4a**).
259 When titrated with the phosphoryl group analog BeF_3^-, both spectra showed extensive chemical
260 shift perturbations, with slow exchange behavior (**Figure 6a**). RT-PhyR′ reached saturation at
261 the highest BeF_3^- titration point, whereas RT-PhyR did not, suggesting weaker binding by RT-
262 PhyR. Similar slow exchange phenomena were observed when titrating RT-NepR′ to each
263 homolog (**Figure 6b**), but only RT-PhyR′ reached saturation at the highest titration point of RT-
264 NepR′. This suggests that RT-PhyR has a lower affinity for RT-NepR′ than RT-PhyR′ does,
265 similar to the BeF_3^- observations. We underscore that the substantial chemical shift
266 perturbations we observed for RT-NepR′ titrations into the apo-forms (i.e. no BeF_3^-) of both

267 PhyR proteins were unexpected, as comparable studies in other PhyR/NepR pairs showed no

268 interaction [24,25,27] or much smaller peak shifts[20,29].

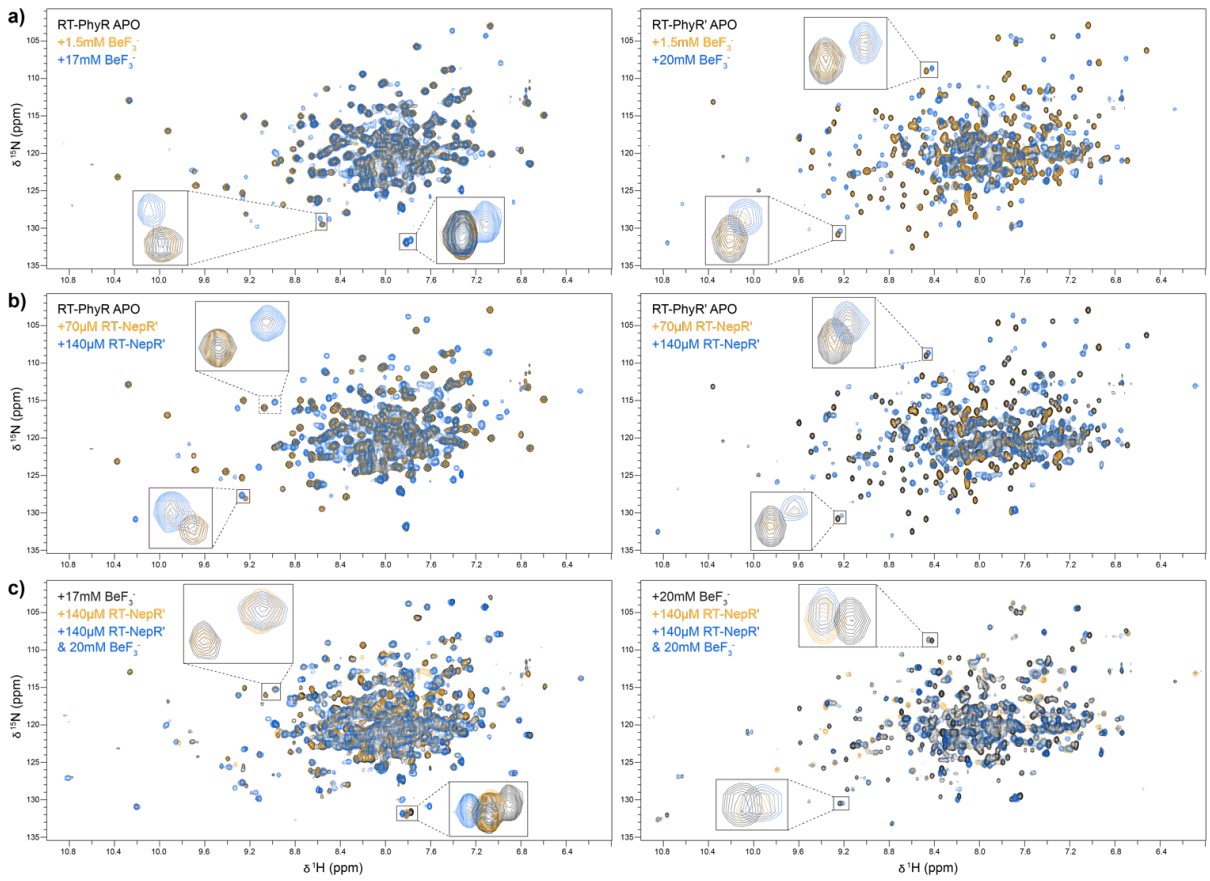

Figure 6: RT-PhyR binds RT-NepR′ and BeF_3^- with positive cooperativity while RT-PhyR′ binds these ligands with negative cooperativity. $^{15}N/^{1}H$ TROSY of 210 μM ^{15}N-labeled RT-PhyR (left) and 220 μM ^{15}N-labeled RT-PhyR′ (right). Proteins were titrated with **a)** BeF_3^-, **b)** RT-NepR′, or **c)** both at concentrations indicated in panel insets. Chemical shift perturbations that best illustrate the effects of each condition are expanded in each panel.

269 To explore the coupling of PhyR proteins binding to BeF_3^- and RT-NepR′, and thus

270 investigate the phosphorylation dependence of this interaction, we titrated BeF_3^- into RT-PhyR

271 or RT-PhyR′ samples that were pre-equilibrated with RT-NepR′ (**Figure 6c**). We observed

272 markedly different results compared to the single titrations above: For RT-PhyR, we saw many

273 peaks shift into positions distinct from those seen when the protein was titrated with either

274 substance alone, indicating a synergistic effect. On the other hand, addition of BeF_3^- to RT-

275 NepR′-equilibrated RT-PhyR′ did not cause any substantial spectral shifts, showing that RT-
276 PhyR′ binds RT-NepR′ to the exclusion of BeF_3^- rather than cooperatively.
277
278 **Discussion**
279 Here we aimed to investigate the unusual features of RT-HK oligomeric state and
280 signaling logic seen in our prior study[34] and to probe interactions between downstream partners.
281 We started with RT-HK itself, using low-resolution limited trypsinolysis to investigate its structure
282 and dynamics in various conditions and nucleotide states (**Figure 1b**). The effect of these
283 conditions on protease accessibility (**Figure 1c**) were reminiscent of those seen for oligomeric
284 state[34], prompting an investigation into the autophosphorylation mechanism of RT-HK.
285 We used mutagenesis to determine that RT-HK uses an *in trans* mechanism (**Figure 1f**).
286 This result was somewhat unexpected based on the AlphaFold model of RT-HK, as prior
287 investigations of the relationship between autophosphorylation mechanism and helix bundle
288 loop handedness in a number of HisKA family systems[54] suggested that the left-handed loop
289 predicted for RT-HK should confer *cis* autophosphorylation. While such a discrepancy may stem
290 from either *bona fide* mechanistic differences or inaccuracies in the AlphaFold prediction, we
291 note that a similar conflict was seen for the His_KA3 family HK DesK, which has an
292 experimentally-solved structure[55,56], leading us to attribute this to the former.
293 RT-HK solvent accessibility was next assessed at the peptide-level using HDX-MS
294 (**Figure 2**). Bimodal distributions were seen for m/z spectra of peptides throughout the LOV
295 domain, indicating the existence of two distinct states/conformations (**Figure S1**). A relatively
296 higher abundance of the fast-exchanging population under lit conditions suggests that a higher
297 proportion of the LOV domain adopts the associated conformation in the light. At the C-terminus
298 of the LOV domain, in the Jα linker helix, exchange increased under lit conditions in the apo and
299 AMP-PNP-bound states. This result is consistent with the widely-held observation that the Jα

300 helix plays a key role in transmitting light-mediated conformational changes[39,48,51,57]. For
301 example, undocking of the Jα from the LOV domain upon illumination has been seen in
302 AsLOV2[48,58,59] and increased accessibility of the Jα helix has been seen in lit-state EL222[49]. Our
303 HDX-MS measurements also highlight that nucleotide is essential for building a light responsive
304 state, as evidenced by changes in the DHp and CA regions upon nucleotide addition. These
305 results are generally comparable to EL346[42], where light-induced changes are also seen
306 throughout the DHp in the nucleotide-bound states. In both cases, an increase in exchange is
307 seen in the helix surrounding the phosphoacceptor histidine. Overall, RT-HK evidently makes
308 use of a signal transduction mechanism similar to other light-activated systems, despite its
309 reversed signaling logic.

310 The role of Jα helix properties in LOV-HK signal transmission has been a focus of many
311 studies involving the chimeric engineered YF1 system[39,51,57], which also exhibits a "dark active,
312 lit inactive" reversed logic. A common theme among these works is the importance of the
313 heptad periodicity of the coiled-coil linker helix between sensory and output modules in defining
314 signaling logic. Though this exact pattern was not found to be applicable to another inverted
315 chimeric light-sensing HK (with a phytochrome-type photosensory module sensor domain)[38],
316 both systems highlight the general importance of the continuous coiled-coil linker. Since the
317 structural model of RT-HK shows a proline-mediated break in its analogous linker, we made
318 systematic deletions to alter the length (and potentially linearize) this region while assessing its
319 role in signal transduction (**Figure 3a**). We saw a clear stepwise change in net dark state
320 activity as single residue deletions were made (**Figure 3c**): Jα1 dropped below WT; Jα2 greatly
321 increased; Jα3 saw a decrease relative to Jα2; and Jα4 exhibited the least activity overall. This
322 pattern is strikingly similar to the periodicity of a coiled coil linker, similar to what has been
323 observed for YF1[39,51,57].

324 To investigate how RT-HK passes its signal to downstream partners, we next sought to
325 identify cognate RR proteins. HWE/HisKA2 family HKs are well-established as sensory proteins
326 in the GSR networks of *Alphaproteobacteria*[13-20]. We discovered that the *R. therm.* genome
327 includes two homologous copies each of the key GSR regulators σ^{EcfG} and PhyR. Since multiple
328 genomic copies of σ^{EcfG} are seen more commonly than PhyR, work elucidating the interplay
329 between paralogs in other organisms[27,32,52] has mostly focused on σ^{EcfG}. Only two studies have
330 addressed systems with multiple PhyR copies, including one in *S. meliloti* (one σ^{EcfG}, two
331 NepRs, and two PhyRs; both NepRs interact with both PhyRs and with the single σ^{EcfG}, but to
332 different extents[27]) and another in *S. granuli* (all three GSR proteins are duplicated; both NepRs
333 interact with both σ^{EcfG} proteins and both PhyRs to varying extents[32]). While some organisms
334 have the same combination of GSR regulators as *R. therm.*[60], they have not been systematically
335 studied to the best of our knowledge. In general though, the combinations of GSR protein
336 copies and interactions among them tend to vary between systems[31,61,62]; an observation
337 consistent with the hypothesis that multiple copies have diverged to assume different regulatory
338 roles.
339 To probe the roles of the GSR paralogs in *R. therm.*, we began with *in vitro*
340 phosphotransfer measurements from RT-HK to both PhyR proteins (**Figure 4b**). These
341 experiments revealed RT-PhyR as the cognate partner and indicated that phosphotransfer was
342 more efficient in the dark state. On the other hand, the level of non-specific phosphotransfer to
343 RT-PhyR′ was not dependent on the dark or lit state of RT-HK, though it seems unlikely to be
344 an *in vivo* substrate regardless. Instead, our data support a model where the dark state signal of
345 RT-HK is further propagated by the action of RT-PhyR.
346 X-ray crystal structures of both PhyR homologs (**Figure 5**) present potential structural
347 bases for two key events: 1) RT-HK specificity (**Figure 4b**) and 2) the anomalies in
348 phosphorylation/RT-NepR′ binding observed in NMR experiments (**Figure 6**). The RT-PhyR

349 structure has typical SL and REC domain folds, as well as density for the typically flexible α4
350 helix. This helix plays a role in NepR binding[23,25,28], acting as a "molecular doorstop" to prevent
351 NepR displacement by the REC domain[21], and adopts distinct positions based on the presence
352 of NepR. Alignment of the RT-PhyR SL domain with PhyR structures from other organisms
353 reveals a shift in this region (**Figure S3**) where its α4 helix is situated between the expected
354 NepR-bound and unbound positions. This could explain the propensity for RT-PhyR (and
355 possibly RT-PhyR′, which had insufficient density for us to model the α4 helix into any of the
356 monomers) to bind RT-NepR′ in their unphosphorylated states (**Figure 6**). However, we are
357 wary of overinterpreting this particular detail, as intermolecular interactions between RT-PhyR
358 molecules in the crystal involve the α4 helix, so this position may be artificially stabilized.
359 Though RT-PhyR′ also adopts typical SL and REC domain folds, its β3 loop-α10 helix is
360 markedly shifted relative to RT-PhyR and PhyRs from various other organisms (**Figure 5d**). We
361 also observed discrepancies in the RT-PhyR′ structure at the residue level (**Figure 5d & S4**),
362 including the "leaning-in" Q193, which decreases the solvent accessibility of the
363 phosphoacceptor D, limiting its ability to be phosphorylated by an HK partner. We note that this
364 site is accessible to BeF_3^- in our NMR experiments, leaving open the potential for small
365 molecule phosphodonors like acetyl phosphate to control the system. The RT-PhyR′ structural
366 shifts also likely play a role in altering signal propagation from the SL to the REC (**Figure S4**).
367 The function of the two PhyR paralogs along subsequent steps of the GSR pathway was
368 assessed in a series of NMR titration experiments. Addition of the phosphoryl group analog
369 BeF_3^- produced substantial chemical shift perturbations in the spectra of both RT-PhyR and RT-
370 PhyR′, indicating widespread conformational changes upon activation (**Figure 6a**). These
371 results appear to support the broadly accepted hypothesis that REC domain phosphorylation
372 produces the PhyR open state necessary for PhyR/NepR complex formation[22-27]. However,
373 additional NMR experiments surprisingly showed large chemical shift perturbations upon

374 addition of RT-NepR′ to both BeF_3^--free PhyRs (**Figure 6b**). These results are consistent with a
375 more complex mechanism, such as the one previously proposed where nascent NepR binding
376 and PhyR phosphorylation act cooperatively to form the inhibitory PhyR~P/NepR complex[29].
377 Indeed, our results for RT-PhyR indicate a synergistic effect expected from such a mechanism.
378 However, the analogous interactions seem to be inverted in RT-PhyR′, (**Figure 6c**), which
379 exclusively binds RT-NepR′ when provided with both RT-NepR′ and BeF_3^-, suggesting a
380 negatively cooperative function for this paralog. Ultimately, *in vivo* confirmation of interactions
381 between GSR proteins and their functional importance will be advantageous, but our
382 biochemical and structural data make strong predictions regarding the differential roles of RT-
383 PhyR and RT-PhyR′.

384 Taken together, our results support the model depicted in **Figure 7**. In the dark, RT-HK
385 increases its net *in trans* autophosphorylation and signals to its cognate partner RT-PhyR much
386 more efficiently than to RT-PhyR′. Still, both proteins adopt distinct conformations upon addition
387 of a phosphoryl group analog. In the absence of phosphorylation, both PhyRs interact
388 extensively with RT-NepR′, each adopting a third conformation. In RT-PhyR, these two

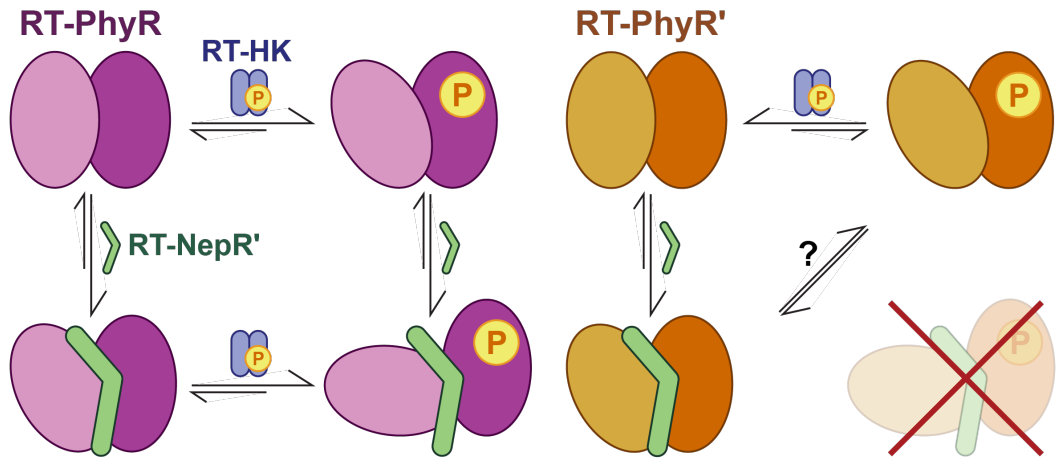

Figure 7: Summary of proposed binding modes for *R. therm.* PhyR homologs. This model illustrates the distinct conformations adopted by RT-PhyR (left) and RT-PhyR′ (right) identified in this study. RT-HK is depicted in blue and RT-NepR′ is in green. The relative sizes of the reaction arrows indicate the equilibrium position.

389 pathways from the unphosphorylated conformation evidently act synergistically to promote
390 formation of the final phosphorylated RT-NepR′-bound complex, as previously proposed for *C.*
391 *crescentus*[29]. In contrast, the absence of a conformation representing the final phosphorylated
392 RT-PhyR′/RT-NepR′ complex strongly suggests a phosphorylation-independent function for this
393 homolog, the details of which remain unclear. All-in-all, these results supplement the existing
394 variety and degree of interactions among copies of GSR regulators. This undoubtedly reflects a
395 wealth of GSR regulatory modes between organisms which have yet to be fully characterized.
396

397 **Experimental Procedures**

398 ***Cloning, protein expression and purification***

399 DNA encoding sequences of RT-HK, RT-PhyR and RT-PhyR′ (NCBI Gene locus tags
400 RUTHE_RS05260, RUTHE_RS05225, and RUTHE_RS12555, respectively) were amplified
401 from *Rubellimicrobium thermophilum* DSM 16684 genomic DNA and Jα deletion genes were
402 ordered from Twist Biosciences. Genes were cloned into the pHis-Gβ1-parallel expression
403 vector[63]. The resulting RT-HK plasmid was used as a template to produce H152A and N256A
404 mutants by site-directed mutagenesis. All constructs were verified by DNA sequencing before
405 being transformed into *Escherichia coli* BL21(DE3) cells (Stratagene). Cells were grown in LB
406 containing 100 µg/mL ampicillin at 37°C and proteins were overexpressed as previously
407 described[42]. Cells were harvested, resuspended in buffer containing 50 mM Tris (pH 8.0), 100
408 mM NaCl, and 10 mM $MgCl_2$, and lysed by sonication. Lysates were centrifuged at 20,000 xg
409 and 4°C for 45 min. Supernatants were filtered through 0.45 µm and bound to a Ni^{2+} Sepharose
410 affinity column (GE Healthcare). The His6-Gβ1 tagged protein was washed with 4 column
411 volumes of cell resuspension buffer supplemented with 20 mM imidazole and eluted with 250
412 mM imidazole. Eluted proteins were incubated with His_6-TEV protease and exchanged into
413 imidazole-deficient buffer by dialysis overnight at 4°C. Proteins were separated from the tags

414 and His_6-TEV protease by Ni^{2+} affinity chromatography and were further purified by size-
415 exclusion chromatography on either a HiLoad 16/600 Superdex 200 pg or a Superdex 200
416 Increase HiScale 16/40 (GE Healthcare) equilibrated with 50 mM Tris (pH 7.0) (for RT-PhyR,
417 RT-PhyR′, and RT-NepR′) or 10 mM MES (pH 6.5) (for RT-HK and mutants), and 100 mM
418 NaCl, 10 mM $MgCl_2$, and 1 mM DTT. For light-sensitive proteins, all purification steps were
419 performed under dim red light. Concentrations were determined from the theoretical absorption
420 coefficient, ε_{280} for PhyRs and RT-NepR', calculated from the sequence using the ExPASy
421 ProtParam server[64], and ε_{446} = 11,800 M^{-1} cm^{-1} for all variations of RT-HK.
422
423 ***Limited trypsinolysis***
424 Reactions were performed on 30 μM RT-HK in a buffer containing 50mM Tris (pH 8.0),
425 100 mM NaCl, 10 mM $MgCl_2$, and 1 mM DTT. Samples of apo and 1.6 mM AMP-PNP-
426 equilibrated proteins were equilibrated in lit and dark conditions. Trypsin was added in a 1:1400
427 ratio to RT-HK, and aliquots were removed to a 4 mM PMSF quench solution at timepoints of 0,
428 0.5, 1, 5, 10, 20, 30, 45, and 60 min. Samples were subjected to SDS-PAGE analysis and
429 visualized using Coomassie blue stain.
430
431 ***Production of H152A/N256A heterodimer***
432 Samples of ~100 μM H152A and N256A mutants in buffer containing 10 mM MES (pH
433 6.5), 100 mM NaCl, 10 mM $MgCl_2$, and 1 mM DTT were mixed and allowed to equilibrate at 4°C
434 for 30 min. The mixture was then added to a dialysis cassette and placed in 500 mL of the same
435 buffer supplemented with 6 M urea and allowed to stir at room temperature for 4 hr. The
436 cassette was then placed into 1 L of the original buffer and stirred overnight at 4°C. The mixture
437 was then reconstituted with 250 μM FMN by 30 min equilibration at 4°C and subsequently
438 separated on a Superdex 200 Increase HiScale 16/40 (GE Healthcare).
439

440 ***Autophosphorylation assays of cis/trans and Jα mutants***

441 Experiments were performed as previously described[10,42]. Reactions contained 20 μM
442 protein (40 μM for the heterodimer) in a buffer of 10 mM HEPES (pH 8.0), 100 mM NaCl, 5 mM
443 $MgCl_2$, 2 mM DTT, and 10% glycerol. A mixture of unlabeled ATP and 10 μCi [γ-^{32}P] ATP was
444 added to each protein to initiate the reaction (final ATP concentration 500 μM). Aliquots were
445 removed at time points of approximately 1, 1.5, 2.5, 4, 8, 6, and 32 min for Jα deletion
446 experiments and 30 min only for cis/trans experiments, then quenched in a 4x SDS-gel loading
447 buffer.

448

449 ***Hydrogen-deuterium exchange mass spectrometry***

450 30 μM RT-HK was prepared in buffer containing 10 mM MES, pH 6.0, 25 mM NaCl, 5
451 mM $MgCl_2$, and 1 mM DTT and incubated in dark or light conditions with 1.6 mM ADP or AMP-
452 PNP for 30 min. Subsequent labeling and quenching was handled by the automated LEAP HDX
453 platform (Trajan). Labeling was initiated in the same buffer prepared with 100% D_2O for a
454 precise amount of time before rapid mixing with a quench buffer containing 2 M GdHCl, 3%
455 acetonitrile, and 1% formic acid at 0°C. Next, samples were digested on a Waters Enzymate
456 BEH Pepsin Column before being eluted through a C18 analytical column (Hypersil Gold, 50
457 mm length × 1 mm diameter, 1.9 μm particle size, Thermo Fisher Scientific) and injected into a
458 Bruker maXis-II ESI-QqTOF high-resolution mass spectrometer. Processing of raw mass
459 spectrometry data files was done with Bruker Compass Data Analysis 5.3 and Biotools 3.2
460 software. Identified peptides were then disambiguated using the PIGEON tool[65]. All data files
461 were then imported into version 3.3 of the HDExaminer software from Sierra Analytics to
462 calculate exchange rate profiles.

463

464 ***Phosphotransfer assays***

465 Phosphotransfer from RT-HK to RT-PhyR and RT-PhyR′ was measured as described
466 previously[24,53]. Reactions took place in a buffer containing 10 mM HEPES (pH 8.0), 100 mM
467 NaCl, 5 mM $MgCl_2$, and 2 mM DTT. A mixture of unlabeled ATP and 24 μCi [γ-^{32}P] ATP was
468 added to RT-HK to initiate autophosphorylation (final ATP concentration 500 μM, and final HK
469 concentration 10 μM). This reaction was allowed to occur for 10 min before a negative control
470 aliquot was placed into 4x SDS-gel loading quench buffer, and the rest was mixed with an equal
471 amount of RR candidate (final concentration both proteins 5 μM). Aliquots of this mixture were
472 removed at 30 s and 10 min timepoints and placed into quench buffer. For dark measurements,
473 all steps were performed under dim red light. For lit measurements, the samples were
474 illuminated with a blue LED panel just prior to and throughout the course of the experiment.
475 Samples were subjected to SDS-PAGE analysis, gels were dried and exposed to a storage
476 phosphoscreen, and bands were visualized by phosphoimaging with a Typhoon FLA 9500 (GE
477 Healthcare).

478

479 ***Crystallization and structure determination of RT-PhyR and RT-PhyR′***

480 Commercially available NeXtal PEGs and ComPAS suite screens were employed to find
481 suitable conditions. Crystals of RT-PhyR and RT-PhyR′ were optimized and grown at room
482 temperature using sitting-drops vapor diffusion method in the presence of 5 and 10 mM $MgCl_2$,
483 respectively. The RT-PhyR crystallization buffer consisted of 16% (w/v) PEG 10000 and 0.1 M
484 Tris (pH 8.5). RT-PhyR′ was crystallized from a solution of 0.2 M KSCN, 20% (w/v) PEG2250,
485 and 0.1 M BIS-TRIS propane (pH 6.0). Resulting crystals were cryoprotected with LV CryoOil
486 (MiTeGen), looped, and flash-cooled in liquid N_2 prior to data collection. Data were collected at
487 the National Synchrotron Light Source II(NSLS-II) light source at Brookhaven National
488 Laboratory using the FMX (17-ID-2) beamline for RT-PhyR and the AMX (17-ID-1) beamline for

489 RT-PhyR′. Data were processed using the autoPROC toolbox[66], resulting in datasets at 1.99 Å
490 (RT-PhyR) and 2.83 Å (RT-PhyR′) resolution. Balbes[67] was used to produce search models,
491 and structures were determined by molecular replacement with Phaser[68]. Several cycles of
492 refinement were conducted using Coot[69] and Phenix[68]. Final data collection, processing, and
493 refinement parameters are provided in **Table S1**.
494
495 ***Titration experiments with BeF_3^- and RT-NepR′***
496 Starting samples contained 215 μM ^{15}N-labeled RT-PhyR and RT-PhyR′ in 50 mM Tris
497 (pH 7.0), 100 mM NaCl, 10 mM $MgCl_2$, and 5% D_2O. These were titrated with BeF_3^- (using a
498 fresh 400 mM stock solution prepared by mixing 400 mM $BeCl_2$ and 1.2 M NaF) to
499 concentrations ranging from 1.5-20 mM, or with RT-NepR′ (using a 220 μM stock solution) to
500 concentrations ranging from 70-140 μM (while RT-PhyR/′ concentrations decreased
501 accordingly). ^{15}N/^{1}H TROSY (^{15}N/^{1}H-WADE-TROSY[70]) spectra were collected at 313.1K on a
502 Bruker Avance III HD spectrometer equipped with a 5mm TCI CryoProbe and operating at a ^{1}H
503 frequency of 800.05 MHz. NMRFx Analyst[71] was used for data processing and analysis.
504
505 *Data availability*— Structure factors and atomic coordinates have been deposited in the Protein
506 Data Bank with PDB IDs 9BY5 and 9CB6.
507
508 *Supporting information* – This article contains supporting information, including Table S1 and
509 Figures S1-2.
510
511 *Acknowledgements* – The authors would like to thank Sean Crosson (Michigan State University)
512 and members of the Gardner Laboratory for useful discussions. We would also like to
513 acknowledge Joseph DiCandia for assistance with figure building and manuscript review. This

research used the AMX and FMX beamlines of the National Synchrotron Light Source II, a U.S. Department of Energy (DOE) Office of Science User Facility operated for the DOE Office of Science by Brookhaven National Laboratory under Contract No. DE-SC0012704. The Center for BioMolecular Structure (CBMS) is primarily supported by the National Institutes of Health, National Institute of General Medical Sciences (NIGMS) through a Center Core P30 Grant (P30 GM133893), and by the DOE Office of Biological and Environmental Research (KP1607011).

Funding and additional information— This work was supported by the National Institutes of Health grants R01 GM106239 (to K.H.G.) and T32 GM136499 (supporting L.E.), and National Science Foundation grant 1852496 (supporting R.A.), and the Mina Rees Dissertation Fellowship from the CUNY Graduate Center (to D.S.). The content is solely the responsibility of the authors and does not necessarily represent the official views of the National Institutes of Health.

Conflicts of interest – The authors declare that they have no conflicts of interest with the contents of this article.

Abbreviations – CA, catalytic ATP-binding; DHp, dimerization histidine phosphotransfer; HK, histidine kinase; GSR, general stress response; HDX-MS, hydrogen-deuterium exchange mass spectrometry; LOV, Light-Oxygen-Voltage; NMR, nuclear magnetic resonance; REC, receiver domain; RR, response regulator; SL, sigma-like domain; TCS, two-component system; TROSY, transverse relaxation-optimized spectroscopy.

References

1. Abramson J, Adler J, Dunger J, Evans R, Green T, Pritzel A, Ronneberger O, Willmore L, Ballard AJ, Bambrick J, Bodenstein SW, Evans DA, Hung CC, O'Neill M, Reiman D, Tunyasuvunakool K, Wu Z, Zemgulyte A, Arvaniti E, Beattie C, Bertolli O, Bridgland A,

541 Cherepanov A, Congreve M, Cowen-Rivers AI, Cowie A, Figurnov M, Fuchs FB, Gladman H,
542 Jain R, Khan YA, Low CMR, Perlin K, Potapenko A, Savy P, Singh S, Stecula A,
543 Thillaisundaram A, Tong C, Yakneen S, Zhong ED, Zielinski M, Zidek A, Bapst V, Kohli P,
544 Jaderberg M, Hassabis D, Jumper JM. Accurate structure prediction of biomolecular interactions
545 with AlphaFold 3. Nature. 2024;630(8016):493-500. Epub 20240508. doi: 10.1038/s41586-024-
546 07487-w. PubMed PMID: 38718835; PMCID: PMC11168924.

547 2. Francez-Charlot A, Kaczmarczyk A, Fischer HM, Vorholt JA. The general stress
548 response in Alphaproteobacteria. Trends in microbiology. 2015;23(3):164-71. Epub 2015/01/15.
549 doi: 10.1016/j.tim.2014.12.006. PubMed PMID: 25582885.

550 3. Mascher T, Helmann JD, Unden G. Stimulus perception in bacterial signal-transducing
551 histidine kinases. Microbiol Mol Biol Rev. 2006;70(4):910-38. Epub 2006/12/13. doi:
552 10.1128/MMBR.00020-06. PubMed PMID: 17158704; PMCID: PMC1698512.

553 4. West AH, Stock AM. Histidine kinases and response regulator proteins in two-
554 component signaling systems. Trends Biochem Sci. 2001;26(6):369-76. Epub 2001/06/19.
555 PubMed PMID: 11406410.

556 5. Wang S. Bacterial Two-Component Systems: Structures and Signaling Mechanisms. In:
557 Huang C, editor. Protein Phosphorylation in Human Health: InTech; 2012.

558 6. Mechaly AE, Soto Diaz S, Sassoon N, Buschiazzo A, Betton JM, Alzari PM. Structural
559 Coupling between Autokinase and Phosphotransferase Reactions in a Bacterial Histidine
560 Kinase. Structure. 2017;25(6):939-44 e3. Epub 2017/05/30. doi: 10.1016/j.str.2017.04.011.
561 PubMed PMID: 28552574.

562 7. Kenney LJ, Anand GS. EnvZ/OmpR Two-Component Signaling: An Archetype System
563 That Can Function Noncanonically. EcoSal Plus. 2020;9(1). Epub 2020/02/01. doi:
564 10.1128/ecosalplus.ESP-0001-2019. PubMed PMID: 32003321; PMCID: PMC7192543.

565 8. Herrou J, Crosson S, Fiebig A. Structure and function of HWE/HisKA2-family sensor
566 histidine kinases. Curr Opin Microbiol. 2017;36:47-54. Epub 2017/02/15. doi:
567 10.1016/j.mib.2017.01.008. PubMed PMID: 28193573; PMCID: PMC5534388.

568 9. Karniol B, Vierstra RD. The HWE histidine kinases, a new family of bacterial two-
569 component sensor kinases with potentially diverse roles in environmental signaling. J Bacteriol.
570 2004;186(2):445-53. Epub 2004/01/02. PubMed PMID: 14702314; PMCID: PMC305753.

571 10. Rivera-Cancel G, Ko WH, Tomchick DR, Correa F, Gardner KH. Full-length structure of
572 a monomeric histidine kinase reveals basis for sensory regulation. Proc Natl Acad Sci U S A.
573 2014;111(50):17839-44. doi: 10.1073/pnas.1413983111. PubMed PMID: 25468971; PMCID:
574 PMC4273353.

575 11. Wojnowska M, Yan J, Sivalingam GN, Cryar A, Gor J, Thalassinos K, Djordjevic S.
576 Autophosphorylation activity of a soluble hexameric histidine kinase correlates with the shift in
577 protein conformational equilibrium. Chem Biol. 2013;20(11):1411-20. Epub 2013/11/12. doi:
578 10.1016/j.chembiol.2013.09.008. PubMed PMID: 24210218; PMCID: PMC3899027.

579 12. Rinaldi J, Arrar M, Sycz G, Cerutti ML, Berguer PM, Paris G, Estrin DA, Marti MA, Klinke
580 S, Goldbaum FA. Structural Insights into the HWE Histidine Kinase Family: The Brucella Blue

581 Light-Activated Histidine Kinase Domain. J Mol Biol. 2016;428(6):1165-79. Epub 2016/02/07.
582 doi: 10.1016/j.jmb.2016.01.026. PubMed PMID: 26851072.

583 13. Staron A, Mascher T. General stress response in alpha-proteobacteria: PhyR and
584 beyond. Mol Microbiol. 2010;78(2):271-7. doi: 10.1111/j.1365-2958.2010.07336.x. PubMed
585 PMID: 20979331.

586 14. Correa F, Ko WH, Ocasio V, Bogomolni RA, Gardner KH. Blue light regulated two-
587 component systems: enzymatic and functional analyses of light-oxygen-voltage (LOV)-histidine
588 kinases and downstream response regulators. Biochemistry. 2013;52(27):4656-66. doi:
589 10.1021/bi400617y. PubMed PMID: 23806044; PMCID: PMC3830641.

590 15. Kaczmarczyk A, Hochstrasser R, Vorholt JA, Francez-Charlot A. Complex two-
591 component signaling regulates the general stress response in Alphaproteobacteria. Proc Natl
592 Acad Sci U S A. 2014;111(48):E5196-204. Epub 2014/11/19. doi: 10.1073/pnas.1410095111.
593 PubMed PMID: 25404331; PMCID: PMC4260549.

594 16. Foreman R, Fiebig A, Crosson S. The LovK-LovR two-component system is a regulator
595 of the general stress pathway in Caulobacter crescentus. J Bacteriol. 2012;194(12):3038-49.
596 Epub 2012/03/13. doi: 10.1128/JB.00182-12. PubMed PMID: 22408156; PMCID: PMC3370868.

597 17. Ocasio VJ, Correa F, Gardner KH. Ligand-induced folding of a two-component signaling
598 receiver domain. Biochemistry. 2015;54(6):1353-63. doi: 10.1021/bi501143b. PubMed PMID:
599 25629646; PMCID: PMC4423417.

600 18. Metzger LC, Francez-Charlot A, Vorholt JA. Single-domain response regulator involved
601 in the general stress response of Methylobacterium extorquens. Microbiology (Reading).
602 2013;159(Pt 6):1067-76. Epub 20130417. doi: 10.1099/mic.0.066068-0. PubMed PMID:
603 23596318.

604 19. Kaczmarczyk A, Hochstrasser R, Vorholt JA, Francez-Charlot A. Two-tiered histidine
605 kinase pathway involved in heat shock and salt sensing in the general stress response of
606 Sphingomonas melonis Fr1. J Bacteriol. 2015;197(8):1466-77. Epub 20150209. doi:
607 10.1128/JB.00019-15. PubMed PMID: 25666137; PMCID: PMC4372748.

608 20. Kim HS, Caswell CC, Foreman R, Roop RM, 2nd, Crosson S. The Brucella abortus
609 general stress response system regulates chronic mammalian infection and is controlled by
610 phosphorylation and proteolysis. J Biol Chem. 2013;288(19):13906-16. doi:
611 10.1074/jbc.M113.459305. PubMed PMID: 23546883; PMCID: PMC3650426.

612 21. Fiebig A, Herrou J, Willett J, Crosson S. General Stress Signaling in the
613 Alphaproteobacteria. Annu Rev Genet. 2015;49:603-25. Epub 2015/10/08. doi:
614 10.1146/annurev-genet-112414-054813. PubMed PMID: 26442844; PMCID: PMC4710059.

615 22. Francez-Charlot A, Frunzke J, Reichen C, Ebneter JZ, Gourion B, Vorholt JA. Sigma
616 factor mimicry involved in regulation of general stress response. Proc Natl Acad Sci U S A.
617 2009;106(9):3467-72. Epub 2009/02/17. doi: 10.1073/pnas.0810291106. PubMed PMID:
618 19218445; PMCID: PMC2642658.

619 23. Herrou J, Foreman R, Fiebig A, Crosson S. A structural model of anti-anti-sigma
620 inhibition by a two-component receiver domain: the PhyR stress response regulator. Mol

621 Microbiol. 2010;78(2):290-304. Epub 2010/08/26. doi: 10.1111/j.1365-2958.2010.07323.x.
622 PubMed PMID: 20735776; PMCID: PMC2959141.

623 24. Correa F, Gardner KH. Basis of Mutual Domain Inhibition in a Bacterial Response
624 Regulator. Cell Chem Biol. 2016;23(8):945-54. doi: 10.1016/j.chembiol.2016.07.010. PubMed
625 PMID: 27524295; PMCID: PMC5159254.

626 25. Campagne S, Damberger FF, Kaczmarczyk A, Francez-Charlot A, Allain FH, Vorholt JA.
627 Structural basis for sigma factor mimicry in the general stress response of Alphaproteobacteria.
628 Proc Natl Acad Sci U S A. 2012;109(21):E1405-14. Epub 2012/05/03. doi:
629 10.1073/pnas.1117003109. PubMed PMID: 22550171; PMCID: PMC3361459.

630 26. Gourion B, Rossignol M, Vorholt JA. A proteomic study of Methylobacterium extorquens
631 reveals a response regulator essential for epiphytic growth. Proc Natl Acad Sci U S A.
632 2006;103(35):13186-91. Epub 2006/08/24. doi: 10.1073/pnas.0603530103. PubMed PMID:
633 16926146; PMCID: PMC1559774.

634 27. Bastiat B, Sauviac L, Bruand C. Dual control of Sinorhizobium meliloti RpoE2 sigma
635 factor activity by two PhyR-type two-component response regulators. J Bacteriol.
636 2010;192(8):2255-65. Epub 20100212. doi: 10.1128/JB.01666-09. PubMed PMID: 20154128;
637 PMCID: PMC2849433.

638 28. Herrou J, Rotskoff G, Luo Y, Roux B, Crosson S. Structural basis of a protein partner
639 switch that regulates the general stress response of alpha-proteobacteria. Proc Natl Acad Sci U
640 S A. 2012;109(21):E1415-23. Epub 2012/05/03. doi: 10.1073/pnas.1116887109. PubMed
641 PMID: 22550172; PMCID: PMC3361416.

642 29. Luebke JL, Eaton DS, Sachleben JR, Crosson S. Allosteric control of a bacterial stress
643 response system by an anti-sigma factor. Mol Microbiol. 2018;107(2):164-79. Epub 20171208.
644 doi: 10.1111/mmi.13868. PubMed PMID: 29052909; PMCID: PMC5760481.

645 30. Jans A, Vercruysse M, Gao S, Engelen K, Lambrichts I, Fauvart M, Michiels J.
646 Canonical and non-canonical EcfG sigma factors control the general stress response in
647 Rhizobium etli. Microbiologyopen. 2013;2(6):976-87. Epub 20131028. doi: 10.1002/mbo3.137.
648 PubMed PMID: 24311555; PMCID: PMC3892343.

649 31. Francez-Charlot A, Frunzke J, Zingg J, Kaczmarczyk A, Vorholt JA. Multiple sigmaEcfG
650 and NepR Proteins Are Involved in the General Stress Response in Methylobacterium
651 extorquens. PLoS One. 2016;11(3):e0152519. Epub 20160330. doi:
652 10.1371/journal.pone.0152519. PubMed PMID: 27028226; PMCID: PMC4814048.

653 32. de Dios R, Santero E, Reyes-Ramirez F. The functional differences between paralogous
654 regulators define the control of the general stress response in Sphingopyxis granuli TFA.
655 Environmental microbiology. 2022;24(4):1918-31. Epub 20220127. doi: 10.1111/1462-
656 2920.15907. PubMed PMID: 35049124; PMCID: PMC9303464.

657 33. Denner EBM, Kolari M, Hoornstra D, Tsitko I, Kampfer P, Busse HJ, Salkinoja-Salonen
658 M. Rubellimicrobium thermophilum gen. nov., sp. nov., a red-pigmented, moderately
659 thermophilic bacterium isolated from coloured slime deposits in paper machines. Int J Syst Evol
660 Microbiol. 2006;56(Pt 6):1355-62. Epub 2006/06/02. doi: 10.1099/ijs.0.63751-0. PubMed PMID:
661 16738114.

662 34. Dikiy I, Swingle D, Toy K, Edupuganti UR, Rivera-Cancel G, Gardner KH. Diversity of
663 function and higher-order structure within HWE sensor histidine kinases. J Biol Chem.
664 2023;299(8):104934. Epub 20230617. doi: 10.1016/j.jbc.2023.104934. PubMed PMID:
665 37331599; PMCID: PMC10359499.

666 35. Swartz TE, Tseng TS, Frederickson MA, Paris G, Comerci DJ, Rajashekara G, Kim JG,
667 Mudgett MB, Splitter GA, Ugalde RA, Goldbaum FA, Briggs WR, Bogomolni RA. Blue-light-
668 activated histidine kinases: two-component sensors in bacteria. Science. 2007;317(5841):1090-
669 3. doi: 10.1126/science.1144306. PubMed PMID: 17717187.

670 36. Crosson S, Rajagopal S, Moffat K. The LOV domain family: photoresponsive signaling
671 modules coupled to diverse output domains. Biochemistry. 2003;42(1):2-10. Epub 2003/01/08.
672 doi: 10.1021/bi026978l. PubMed PMID: 12515534.

673 37. Fiebig A, Varesio LM, Alejandro Navarreto X, Crosson S. Regulation of the
674 Erythrobacter litoralis DSM 8509 general stress response by visible light. Mol Microbiol.
675 2019;112(2):442-60. Epub 2019/05/28. doi: 10.1111/mmi.14310. PubMed PMID: 31125464;
676 PMCID: PMC6703928.

677 38. Meier SSM, Multamaki E, Ranzani AT, Takala H, Moglich A. Leveraging the histidine
678 kinase-phosphatase duality to sculpt two-component signaling. Nature communications.
679 2024;15(1):4876. Epub 20240610. doi: 10.1038/s41467-024-49251-8. PubMed PMID:
680 38858359; PMCID: PMC11164954.

681 39. Moglich A, Ayers RA, Moffat K. Design and signaling mechanism of light-regulated
682 histidine kinases. J Mol Biol. 2009;385(5):1433-44. Epub 2008/12/27. doi:
683 10.1016/j.jmb.2008.12.017. PubMed PMID: 19109976; PMCID: PMC3527124.

684 40. Rinaldi J, Gallo M, Klinke S, Paris G, Bonomi HR, Bogomolni RA, Cicero DO, Goldbaum
685 FA. The beta-scaffold of the LOV domain of the Brucella light-activated histidine kinase is a key
686 element for signal transduction. J Mol Biol. 2012;420(1-2):112-27. Epub 20120411. doi:
687 10.1016/j.jmb.2012.04.006. PubMed PMID: 22504229.

688 41. Lindner R, Heintz U, Winkler A. Applications of hydrogen deuterium exchange (HDX) for
689 the characterization of conformational dynamics in light-activated photoreceptors. Front Mol
690 Biosci. 2015;2:33. doi: 10.3389/fmolb.2015.00033. PubMed PMID: 26157802; PMCID:
691 PMC4477167.

692 42. Dikiy I, Edupuganti UR, Abzalimov RR, Borbat PP, Srivastava M, Freed JH, Gardner KH.
693 Insights into histidine kinase activation mechanisms from the monomeric blue light sensor
694 EL346. Proc Natl Acad Sci U S A. 2019;116(11):4963-72. Epub 2019/02/28. doi:
695 10.1073/pnas.1813586116. PubMed PMID: 30808807; PMCID: PMC6421462.

696 43. Engelhard C, Diensthuber RP, Moglich A, Bittl R. Blue-light reception through quaternary
697 transitions. Sci Rep. 2017;7(1):1385. Epub 2017/05/05. doi: 10.1038/s41598-017-01497-7.
698 PubMed PMID: 28469162; PMCID: PMC5431215.

699 44. Berntsson O, Diensthuber RP, Panman MR, Bjorling A, Gustavsson E, Hoernke M,
700 Hughes AJ, Henry L, Niebling S, Takala H, Ihalainen JA, Newby G, Kerruth S, Heberle J, Liebi
701 M, Menzel A, Henning R, Kosheleva I, Moglich A, Westenhoff S. Sequential conformational
702 transitions and alpha-helical supercoiling regulate a sensor histidine kinase. Nat Commun.

703 2017;8(1):284. Epub 20170818. doi: 10.1038/s41467-017-00300-5. PubMed PMID: 28819239;
704 PMCID: PMC5561222.

705 45. Möglich A. Signal transduction in photoreceptor histidine kinases. Protein Sci.
706 2019;28(11):1923-46. Epub 2019/08/10. doi: 10.1002/pro.3705. PubMed PMID: 31397927;
707 PMCID: PMC6798134.

708 46. Ninfa EG, Atkinson MR, Kamberov ES, Ninfa AJ. Mechanism of autophosphorylation of
709 Escherichia coli nitrogen regulator II (NRII or NtrB): trans-phosphorylation between subunits. J
710 Bacteriol. 1993;175(21):7024-32. Epub 1993/11/01. PubMed PMID: 8226644; PMCID:
711 PMC206830.

712 47. Madeira F, Madhusoodanan N, Lee J, Eusebi A, Niewielska A, Tivey ARN, Lopez R,
713 Butcher S. The EMBL-EBI Job Dispatcher sequence analysis tools framework in 2024. Nucleic
714 Acids Res. 2024;52(W1):W521-W5. doi: 10.1093/nar/gkae241. PubMed PMID: 38597606;
715 PMCID: PMC11223882.

716 48. Harper SM, Neil LC, Gardner KH. Structural basis of a phototropin light switch. Science.
717 2003;301(5639):1541-4. doi: 10.1126/science.1086810. PubMed PMID: 12970567.

718 49. Nash AI, McNulty R, Shillito ME, Swartz TE, Bogomolni RA, Luecke H, Gardner KH.
719 Structural basis of photosensitivity in a bacterial light-oxygen-voltage/helix-turn-helix (LOV-HTH)
720 DNA-binding protein. Proc Natl Acad Sci U S A. 2011;108(23):9449-54. doi:
721 10.1073/pnas.1100262108. PubMed PMID: 21606338; PMCID: PMC3111320.

722 50. Vide U, Kasapovic D, Fuchs M, Heimböck MP, Totaro MG, Zenzmaier E, Winkler A.
723 Illuminating the inner workings of a natural protein switch: Blue-light sensing in LOV-activated
724 diguanylate cyclases. Sci Adv. 2023;9(31). doi: ARTN eadh4721
725 10.1126/sciadv.adh4721. PubMed PMID: WOS:001041574600001.

726 51. Diensthuber RP, Bommer M, Gleichmann T, Moglich A. Full-length structure of a sensor
727 histidine kinase pinpoints coaxial coiled coils as signal transducers and modulators. Structure.
728 2013;21(7):1127-36. doi: 10.1016/j.str.2013.04.024. PubMed PMID: 23746806.

729 52. Lourenco RF, Kohler C, Gomes SL. A two-component system, an anti-sigma factor and
730 two paralogous ECF sigma factors are involved in the control of general stress response in
731 Caulobacter crescentus. Mol Microbiol. 2011;80(6):1598-612. Epub 2011/05/14. doi:
732 10.1111/j.1365-2958.2011.07668.x. PubMed PMID: 21564331.

733 53. Laub MT, Biondi EG, Skerker JM. Phosphotransfer profiling: systematic mapping of two-
734 component signal transduction pathways and phosphorelays. Methods Enzymol. 2007;423:531-
735 48. Epub 2007/07/05. doi: 10.1016/S0076-6879(07)23026-5. PubMed PMID: 17609150.

736 54. Ashenberg O, Keating AE, Laub MT. Helix bundle loops determine whether histidine
737 kinases autophosphorylate in cis or in trans. J Mol Biol. 2013;425(7):1198-209. doi:
738 10.1016/j.jmb.2013.01.011. PubMed PMID: 23333741; PMCID: PMC3636764.

739 55. Trajtenberg F, Grana M, Ruetalo N, Botti H, Buschiazzo A. Structural and enzymatic
740 insights into the ATP binding and autophosphorylation mechanism of a sensor histidine kinase.
741 The Journal of biological chemistry. 2010;285(32):24892-903. Epub 20100527. doi:
742 10.1074/jbc.M110.147843. PubMed PMID: 20507988; PMCID: PMC2915725.

743 56. Zschiedrich CP, Keidel V, Szurmant H. Molecular Mechanisms of Two-Component
744 Signal Transduction. J Mol Biol. 2016;428(19):3752-75. Epub 20160809. doi:
745 10.1016/j.jmb.2016.08.003. PubMed PMID: 27519796; PMCID: PMC5023499.

746 57. Ohlendorf R, Schumacher CH, Richter F, Moglich A. Library-Aided Probing of Linker
747 Determinants in Hybrid Photoreceptors. ACS Synth Biol. 2016;5(10):1117-26. Epub 20160329.
748 doi: 10.1021/acssynbio.6b00028. PubMed PMID: 27002379.

749 58. Harper SM, Christie JM, Gardner KH. Disruption of the LOV-Jalpha helix interaction
750 activates phototropin kinase activity. Biochemistry. 2004;43(51):16184-92. Epub 2004/12/22.
751 doi: 10.1021/bi048092i. PubMed PMID: 15610012.

752 59. Halavaty AS, Moffat K. N- and C-terminal flanking regions modulate light-induced signal
753 transduction in the LOV2 domain of the blue light sensor phototropin 1 from Avena sativa.
754 Biochemistry. 2007;46(49):14001-9. Epub 2007/11/16. doi: 10.1021/bi701543e. PubMed PMID:
755 18001137.

756 60. Paysan-Lafosse T, Blum M, Chuguransky S, Grego T, Pinto BL, Salazar GA, Bileschi
757 ML, Bork P, Bridge A, Colwell L, Gough J, Haft DH, Letunic I, Marchler-Bauer A, Mi H, Natale
758 DA, Orengo CA, Pandurangan AP, Rivoire C, Sigrist CJA, Sillitoe I, Thanki N, Thomas PD,
759 Tosatto SCE, Wu CH, Bateman A. InterPro in 2022. Nucleic Acids Res. 2023;51(D1):D418-D27.
760 doi: 10.1093/nar/gkac993. PubMed PMID: 36350672; PMCID: PMC9825450.

761 61. Gottschlich L, Geiser P, Bortfeld-Miller M, Field CM, Vorholt JA. Complex general stress
762 response regulation in Sphingomonas melonis Fr1 revealed by transcriptional analyses.
763 Scientific reports. 2019;9(1):9404. Epub 20190628. doi: 10.1038/s41598-019-45788-7. PubMed
764 PMID: 31253827; PMCID: PMC6599016.

765 62. Kaczmarczyk A, Campagne S, Danza F, Metzger LC, Vorholt JA, Francez-Charlot A.
766 Role of Sphingomonas sp. strain Fr1 PhyR-NepR-sigmaEcfG cascade in general stress
767 response and identification of a negative regulator of PhyR. J Bacteriol. 2011;193(23):6629-38.
768 Epub 20110923. doi: 10.1128/JB.06006-11. PubMed PMID: 21949070; PMCID: PMC3232908.

769 63. Sheffield P, Garrard S, Derewenda Z. Overcoming expression and purification problems
770 of RhoGDI using a family of "parallel" expression vectors. Protein Expr Purif. 1999;15(1):34-9.
771 Epub 1999/02/20. doi: 10.1006/prep.1998.1003. PubMed PMID: 10024467.

772 64. Gasteiger E, Hoogland C, Gattiker A, Duvaud Se, Wilkins MR, Appel RD, Bairoch A.
773 Protein Identification and Analysis Tools on the ExPASy Server. In: Walker JM, editor. The
774 Proteomics Protocols Handbook. Totowa, NJ: Humana Press; 2005. p. 571-607.

775 65. Chenlin Lu MLW, Andrew Reckers, Anum Glasgow. Site-resolved energetic information
776 from HX/MS experiments. bioRxiv. 2024.

777 66. Vonrhein C, Flensburg C, Keller P, Sharff A, Smart O, Paciorek W, Womack T, Bricogne
778 G. Data processing and analysis with the autoPROC toolbox. Acta Crystallogr D Biol
779 Crystallogr. 2011;67(Pt 4):293-302. Epub 20110318. doi: 10.1107/S0907444911007773.
780 PubMed PMID: 21460447; PMCID: PMC3069744.

781 67. Agirre J, Atanasova M, Bagdonas H, Ballard CB, Basle A, Beilsten-Edmands J, Borges
782 RJ, Brown DG, Burgos-Marmol JJ, Berrisford JM, Bond PS, Caballero I, Catapano L,

783 Chojnowski G, Cook AG, Cowtan KD, Croll TI, Debreczeni JE, Devenish NE, Dodson EJ,
784 Drevon TR, Emsley P, Evans G, Evans PR, Fando M, Foadi J, Fuentes-Montero L, Garman EF,
785 Gerstel M, Gildea RJ, Hatti K, Hekkelman ML, Heuser P, Hoh SW, Hough MA, Jenkins HT,
786 Jimenez E, Joosten RP, Keegan RM, Keep N, Krissinel EB, Kolenko P, Kovalevskiy O, Lamzin
787 VS, Lawson DM, Lebedev AA, Leslie AGW, Lohkamp B, Long F, Maly M, McCoy AJ,
788 McNicholas SJ, Medina A, Millan C, Murray JW, Murshudov GN, Nicholls RA, Noble MEM,
789 Oeffner R, Pannu NS, Parkhurst JM, Pearce N, Pereira J, Perrakis A, Powell HR, Read RJ,
790 Rigden DJ, Rochira W, Sammito M, Sanchez Rodriguez F, Sheldrick GM, Shelley KL, Simkovic
791 F, Simpkin AJ, Skubak P, Sobolev E, Steiner RA, Stevenson K, Tews I, Thomas JMH, Thorn A,
792 Valls JT, Uski V, Uson I, Vagin A, Velankar S, Vollmar M, Walden H, Waterman D, Wilson KS,
793 Winn MD, Winter G, Wojdyr M, Yamashita K. The CCP4 suite: integrative software for
794 macromolecular crystallography. Acta Crystallogr D Struct Biol. 2023;79(Pt 6):449-61. Epub
795 20230530. doi: 10.1107/S2059798323003595. PubMed PMID: 37259835; PMCID:
796 PMC10233625.

797 68. Liebschner D, Afonine PV, Baker ML, Bunkoczi G, Chen VB, Croll TI, Hintze B, Hung
798 LW, Jain S, McCoy AJ, Moriarty NW, Oeffner RD, Poon BK, Prisant MG, Read RJ, Richardson
799 JS, Richardson DC, Sammito MD, Sobolev OV, Stockwell DH, Terwilliger TC, Urzhumtsev AG,
800 Videau LL, Williams CJ, Adams PD. Macromolecular structure determination using X-rays,
801 neutrons and electrons: recent developments in Phenix. Acta Crystallogr D Struct Biol.
802 2019;75(Pt 10):861-77. Epub 20191002. doi: 10.1107/S2059798319011471. PubMed PMID:
803 31588918; PMCID: PMC6778852.

804 69. Emsley P, Lohkamp B, Scott WG, Cowtan K. Features and development of Coot. Acta
805 Crystallogr D Biol Crystallogr. 2010;66(Pt 4):486-501. Epub 20100324. doi:
806 10.1107/S0907444910007493. PubMed PMID: 20383002; PMCID: PMC2852313.

807 70. Manu VS, Olivieri C, Pavuluri K, Veglia G. Design and applications of water irradiation
808 devoid RF pulses for ultra-high field biomolecular NMR spectroscopy. Phys Chem Chem Phys.
809 2022;24(31):18477-81. Epub 20220810. doi: 10.1039/d2cp01744j. PubMed PMID: 35895081;
810 PMCID: PMC9578148.

811 71. Norris M, Fetler B, Marchant J, Johnson BA. NMRFx Processor: a cross-platform NMR
812 data processing program. J Biomol NMR. 2016;65(3-4):205-16. Epub 20160725. doi:
813 10.1007/s10858-016-0049-6. PubMed PMID: 27457481; PMCID: PMC4983292.
814

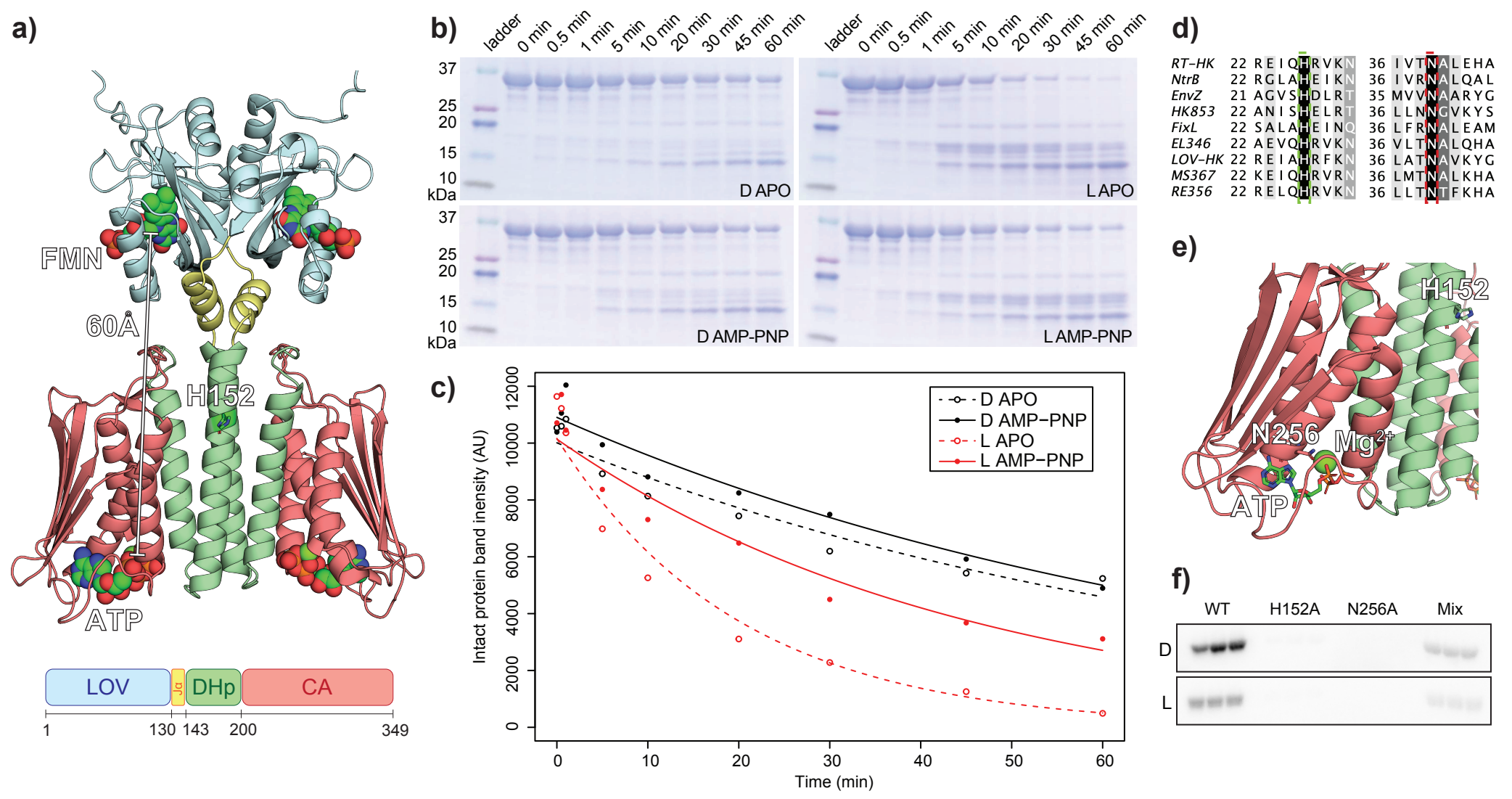
a)
FMN
60Å
H152
ATP
LOV
Jα
DHp
CA
1
130
143
200
349
b)
ladder
0 min
0.5 min
1 min
5 min
10 min
20 min
30 min
45 min
60 min
37
25
20
15
10
kDa
D APO
L APO
D AMP-PNP
L AMP-PNP
c)
D APO
D AMP-PNP
L APO
L AMP-PNP
Intact protein band inensity (AU)
Time (min)
d)
RT-HK 22 REIQHRVKN 36 IVTNALEHA
NtrB 22 RGLAHEIKN 36 IVRNALQAL
EnvZ 21 AGVSHDLRT 35 MVVNAARYG
HK853 22 ANISHELRT 36 LLNNGVKYS
FixL 22 SALAHEINQ 36 LFRNALEAM
EL346 22 AEVQHRVKN 36 VLTNALQHA
LOV-HK 22 REIAHRFKN 36 LATNAVKYG
MS367 22 KEIQHRVRN 36 LMTNALKHA
RE356 22 RELQHRVKN 36 LLTNTFKHA
e)
H152
N256
Mg2+
ATP
f)
WT
H152A
N256A
Mix
D
L

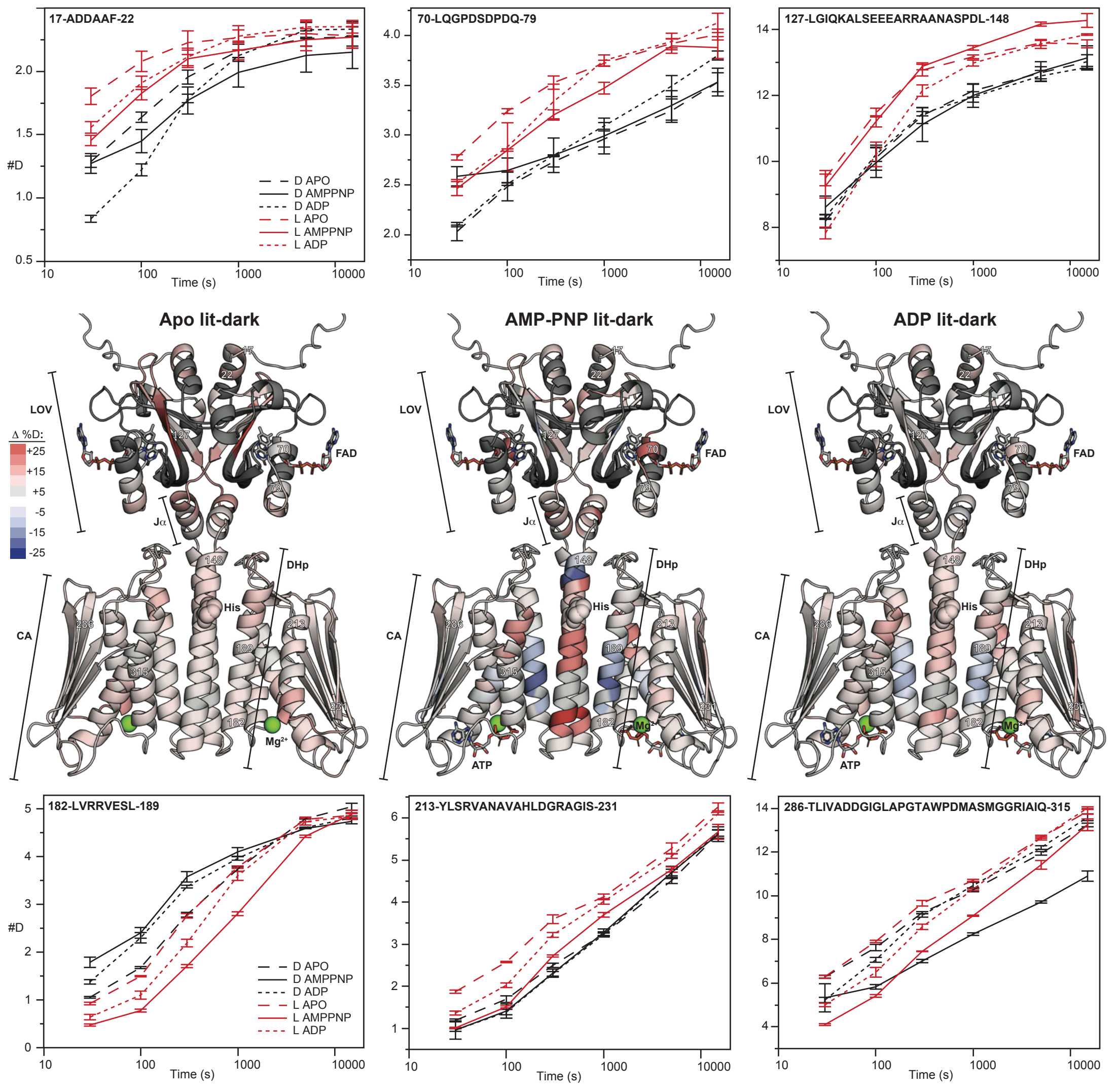
17-ADDAAF-22
70-LQGPDSDPDQ-79
127-LGIQKALSEEEARRAANASPDL-148
#D
Time (s)
D APO
D AMPPNP
D ADP
L APO
L AMPPNP
L ADP
Apo lit-dark
AMP-PNP lit-dark
ADP lit-dark
LOV
FAD
Jα
DHp
CA
His
ATP
Mg2+
Δ %D:
+25
+15
+5
-5
-15
-25
182-LVRRVESL-189
213-YLSRVANAVAHLDGRAGIS-231
286-TLIVADDGIGLAPGTAWPDMASMGGRIAIQ-315

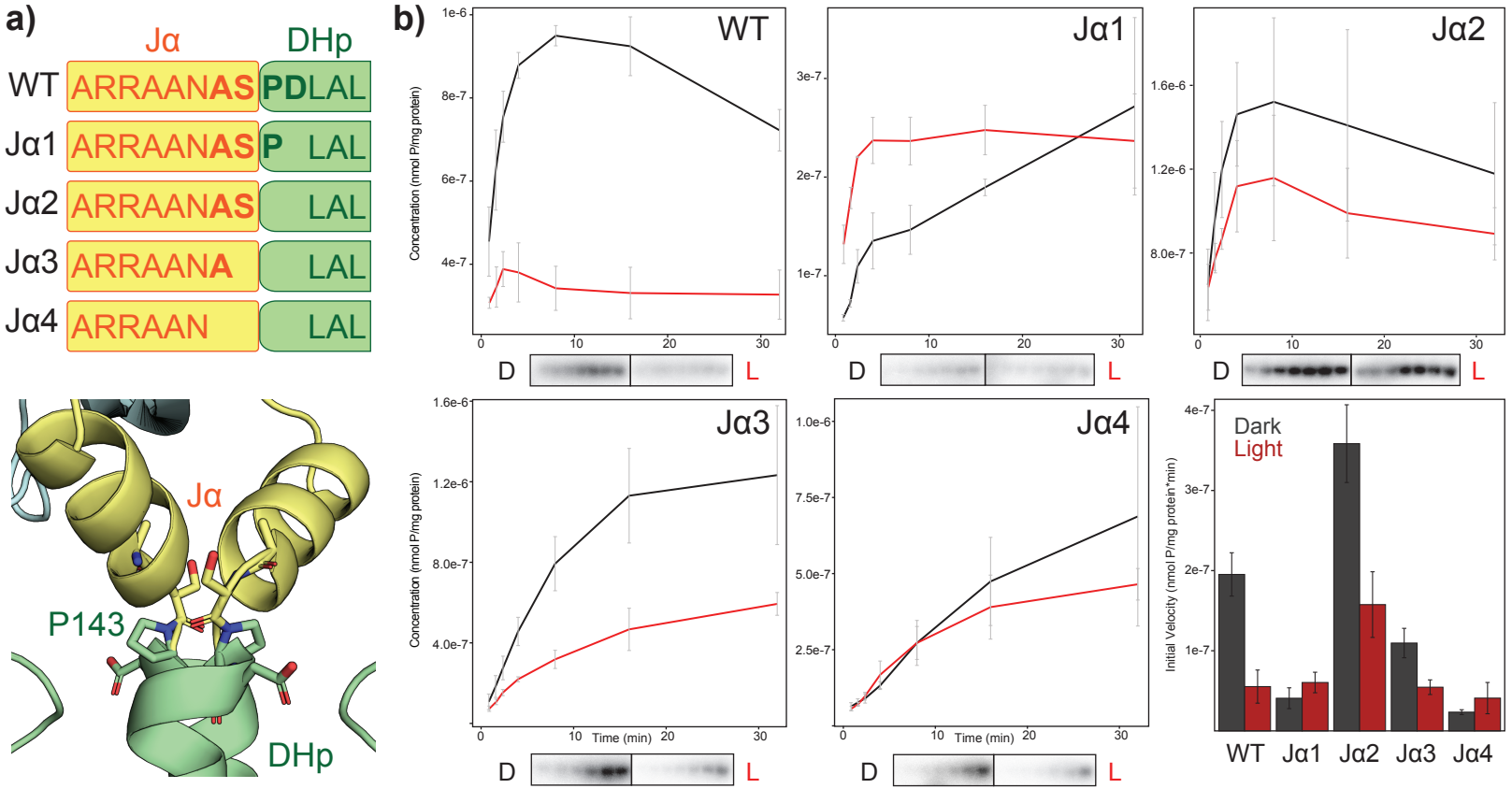
a)
Jα
DHp
WT
ARRAANAS
PDLAL
Jα1
ARRAANAS
P LAL
Jα2
ARRAANAS
LAL
Jα3
ARRAANA
LAL
Jα4
ARRAAN
LAL
Jα
P143
DHp
b)
WT
Jα1
Jα2
Jα3
Jα4
Concentration (nmol P/mg protein)
Time (min)
D
L
Dark
Light
Initial Velocity (nmol P/mg protein*min)
WT
Jα1
Jα2
Jα3
Jα4

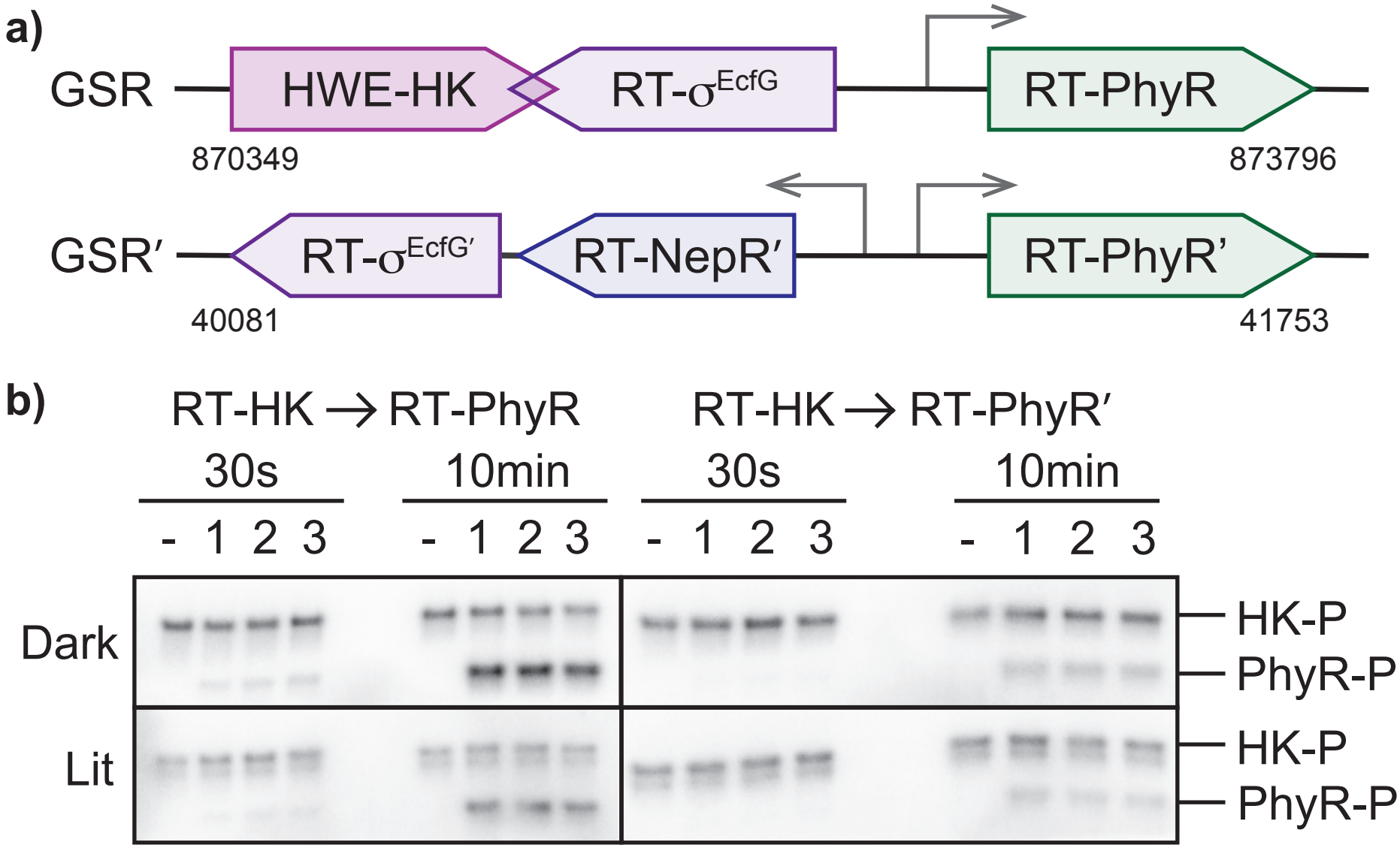
a)
GSR
HWE-HK
RT-σEcfG
RT-PhyR
870349
873796
GSR′
RT-σEcfG′
RT-NepR′
RT-PhyR’
40081
41753
b)
RT-HK → RT-PhyR
RT-HK → RT-PhyR′
30s
10min
30s
10min
- 1 2 3
- 1 2 3
- 1 2 3
- 1 2 3
Dark
Lit
HK-P
PhyR-P
HK-P
PhyR-P

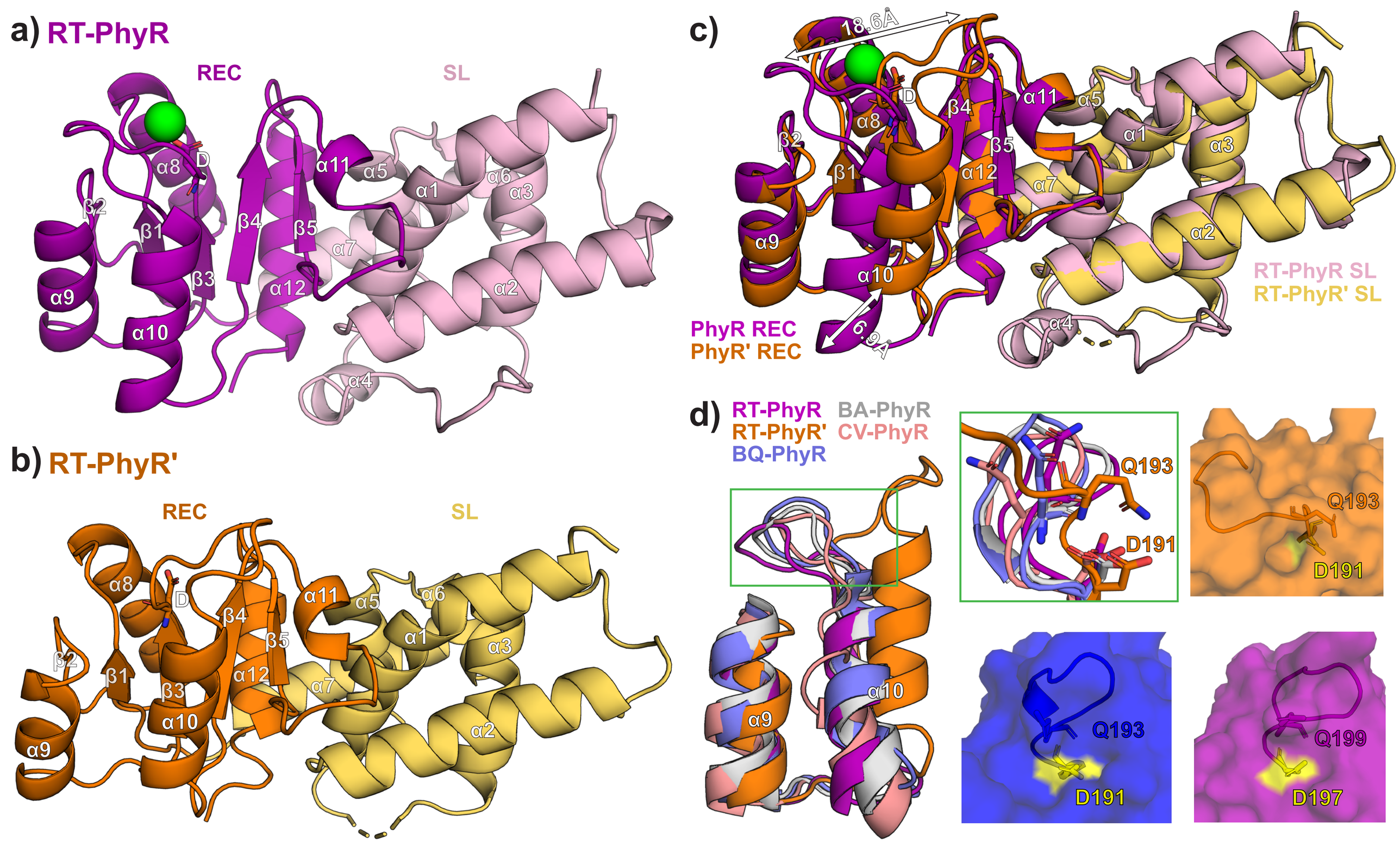
a) RT-PhyR
REC
SL
α8
D
β2
β1
β3
β4
β5
α11
α5
α1
α6
α3
α7
α12
α2
α9
α10
α4
b) RT-PhyR'
REC
SL
α8
D
β2
β1
β3
β4
β5
α11
α5
α6
α1
α3
α7
α12
α2
α9
α10
c)
18.6Å
D
α8
β2
β1
β4
β5
α11
α5
α1
α3
α12
α7
α2
α9
α10
α4
6.9Å
PhyR REC
PhyR' REC
RT-PhyR SL
RT-PhyR' SL
d)
RT-PhyR
RT-PhyR'
BQ-PhyR
BA-PhyR
CV-PhyR
α9
α10
Q193
D191
Q193
D191
Q193
D191
Q199
D197

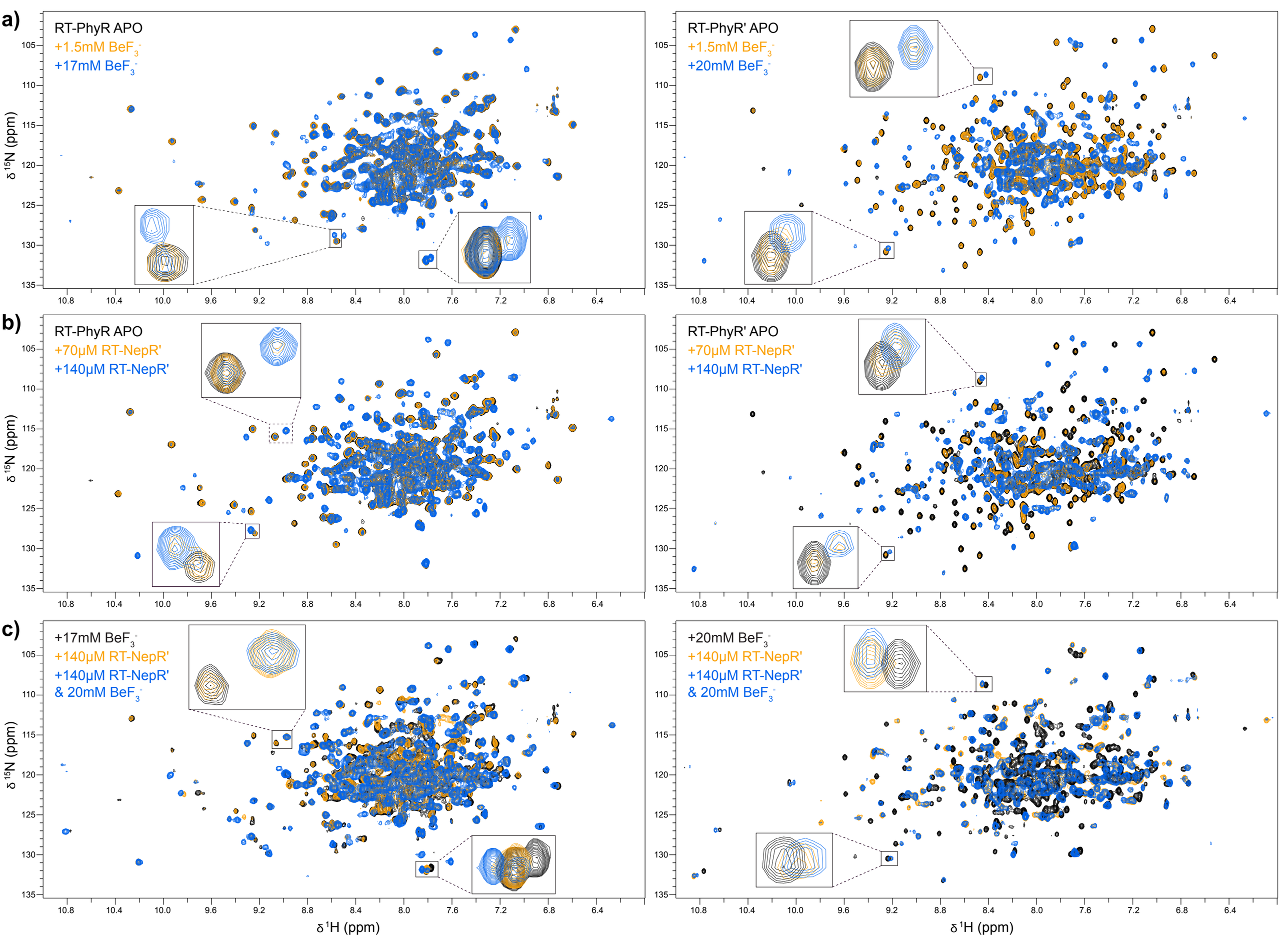
a)
RT-PhyR APO
+1.5mM BeF3-
+17mM BeF3-
RT-PhyR' APO
+1.5mM BeF3-
+20mM BeF3-
b)
RT-PhyR APO
+70µM RT-NepR'
+140µM RT-NepR'
RT-PhyR' APO
+70µM RT-NepR'
+140µM RT-NepR'
c)
+17mM BeF3-
+140µM RT-NepR'
+140µM RT-NepR'
& 20mM BeF3-
+20mM BeF3-
+140µM RT-NepR'
+140µM RT-NepR'
& 20mM BeF3-
δ 15N (ppm)
δ 1H (ppm)

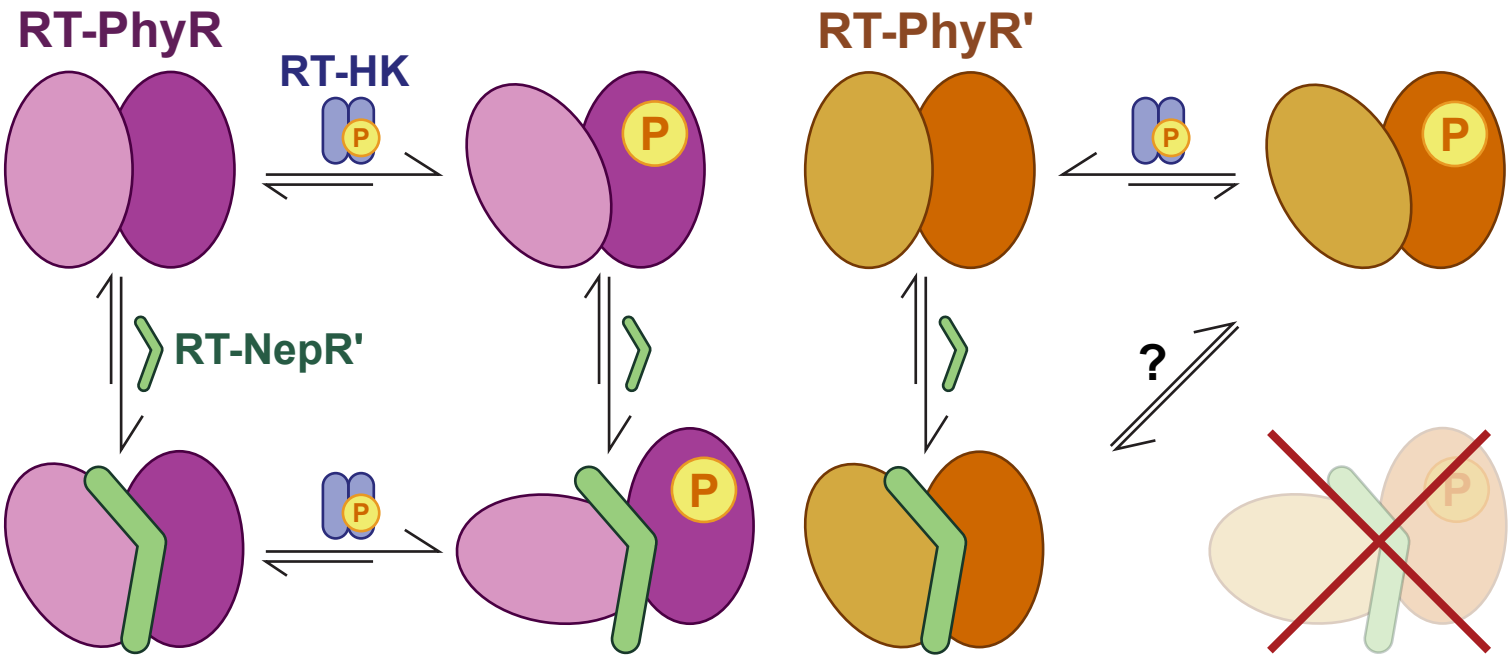
RT-PhyR
RT-HK
P
P
RT-PhyR'
P
RT-NepR'
?
P
P
P